JOURNAL OF GEOPHYSICAL RESEARCH, VOL. 108, NO. D20, 8805, doi:10.1029/2002JD003290, 2003

Large-scale ozone and aerosol distributions, air mass characteristics, and ozone fluxes over the western Pacific Ocean in late winter/early spring

Edward V. Browell,[1] Marta A. Fenn,[2] Carolyn F. Butler,[2] William B. Grant,[1] Vincent G. Brackett,[2] Johnathan W. Hair,[1] Melody A. Avery,[1] Reginald E. Newell,[3,13] Yuanlong Hu,[3] Henry E. Fuelberg,[4] Daniel J. Jacob,[5] Bruce E. Anderson,[1] Elliot L. Atlas,[6] Donald R. Blake,[7] William H. Brune,[8] Jack E. Dibb,[9] Alan Fried,[6] Brian G. Heikes,[10] Glen W. Sachse,[1] Scott T. Sandholm,[11] Hanwant B. Singh,[12] Robert W. Talbot,[9] Stephanie A. Vay,[1] Rodney J. Weber,[11] and Karen B. Bartlett[9]

Received 5 December 2002; revised 3 April 2003; accepted 17 April 2003; published 3 September 2003.

[1] Large-scale measurements of ozone (O_3) and aerosol distributions were made from the NASA DC-8 aircraft during the Transport and Chemical Evolution over the Pacific (TRACE-P) field experiment conducted in February–April 2001. Remote measurements were made with an airborne lidar to provide O_3 and multiple-wavelength aerosol backscatter profiles from near the surface to above the tropopause along the flight track. In situ measurements of O_3, aerosols, and a wide range of trace gases were made onboard the DC-8. Five-day backward trajectories were used in conjunction with the O_3 and aerosol distributions on each flight to indicate the possible origin of observed air masses, such as from biomass burning regions, continental pollution, desert regions, and oceanic regions. Average latitudinal O_3 and aerosol scattering ratio distributions were derived from all flights west of 150°E, and these distributions showed the average latitude and altitude dependence of different dynamical and chemical processes in determining the atmospheric composition over the western Pacific. TRACE-P (TP) showed an increase in the average latitudinal distributions of both O_3 and aerosols compared to PEM-West B (PWB), which was conducted in February–March 1994. O_3, aerosol, and potential vorticity levels were used to identify nine air mass types and quantify their frequency of occurrence as a function of altitude. This paper discusses the characteristics of the different air mass types encountered during TP and compares them to PWB. These results confirmed that most of the O_3 increase in TP was due to photochemistry. The average latitudinal eastward O_3 flux in the western Pacific during TP was found to peak near 32°N with a total average O_3 flux between 14 and 46°N of 5.2 Tg/day. The eastward total CO flux was calculated to be 2.2 Tg-C/day with ~6% estimated from Asia. The Asian flux of CO_2 and CH_4 was estimated at 4.9 and 0.06 Tg-C/day. *INDEX TERMS:* 0365 Atmospheric Composition and Structure: Troposphere—composition and chemistry; 0368 Atmospheric Composition and Structure: Troposphere—constituent transport and chemistry; 0305 Atmospheric Composition and Structure: Aerosols and particles (0345, 4801); 3362 Meteorology and Atmospheric Dynamics: Stratosphere/troposphere interactions; *KEYWORDS:* ozone, aerosols, fluxes, air mass characteristics, western Pacific, TRACE-P

[1]Atmospheric Sciences, NASA Langley Research Center, Hampton, Virginia, USA.
[2]Science Applications International Corporation, Hampton, Virginia, USA.
[3]Department of Earth, Atmospheric, and Planetary Sciences, Massachusetts Institute of Technology, Cambridge, Massachusetts, USA.
[4]Department of Meteorology, Florida State University, Tallahassee, Florida, USA.
[5]Department of Earth and Planetary Science, Harvard University, Cambridge, Massachusetts, USA.
[6]Atmospheric Chemistry Division, National Center for Atmospheric Research, Boulder, Colorado, USA.
[7]Department of Chemistry, University of California, Irvine, California, USA.
[8]Department of Meteorology, Pennsylvania State University, University Park, Pennsylvania, USA.
[9]Institute for the Study of Earth, Oceans, and Space, University of New Hampshire, Durham, New Hampshire, USA.
[10]Graduate School of Oceanography, University of Rhode Island, Narragansett, Rhode Island, USA.
[11]Department of Earth and Atmospheric Sciences, Georgia Institute of Technology, Atlanta, Georgia, USA.
[12]NASA Ames Research Center, Moffett Field, California, USA.
[13]Deceased.

0148-0227/03/2002JD003290

Citation: Browell, E. V., et al., Large-scale ozone and aerosol distributions, air mass characteristics, and ozone fluxes over the western Pacific Ocean in late winter/early spring, *J. Geophys. Res.*, *108*(D20), 8805, doi:10.1029/2002JD003290, 2003.

1. Introduction

[2] The Transport and Chemical Evolution over the Pacific (TRACE-P) field experiment was conducted from 26 February to 9 April 2001 over the Pacific Ocean with flights from Edwards Air Force Base, California, Guam, Hong Kong, Tokyo, and Kona, Hawaii [*Jacob et al.*, 2003]. The objectives of TRACE-P (TP) were to determine the pathways for outflow of chemically and radiatively important gases and aerosols and their precursors from eastern Asia to the western Pacific [*Fuelberg et al.*, 2003; *Koike et al.*, 2003; *Liu et al.*, 2003]; to determine the chemical evolution of the Asian outflow over the western Pacific [*Pierce et al.*, 2003]; and to understand the ensemble of processes that control this evolution [*Lefer et al.*, 2003]. TP was preceded by two exploratory airborne field experiments, Pacific Exploratory Missions (PEM), conducted over the western Pacific during the late summer of 1991 (PEM West-A (PWA)) [*Hoell et al.*, 1996] and the late winter of 1994 (PEM West B (PWB)) [*Hoell et al.*, 1997]. The objectives of these field experiments were to detect and study the Asian outflow in times of weak and strong outflow, respectively. These field experiments revealed the seasonal and spatial variability in the outflow from Asia and the various air mass characteristics observed during these different seasons [*Browell et al.*, 1996a; *Hoell et al.*, 1996, 1997; *Fenn et al.*, 1997]. Since the time of PWB, increased interest in the origin, chemistry, and fate of pollution emerging from the Asian continent [*Jacob et al.*, 1999; *Jaffe*, 1999; *Mauzerall et al.*, 2000; *Staudt et al.*, 2001; *Liu et al.*, 2002] and the anticipated growth in the level of pollution in coming decades [*Streets et al.*, 1999] led to the more focused objectives of the TP field experiment.

[3] During TP, the NASA Langley airborne UV DIAL (Differential Absorption Lidar) system was flown on the NASA DC-8 aircraft and operated simultaneously in the nadir and zenith modes to collectively measure vertical profiles of O_3, aerosols, and clouds from near the surface to the upper troposphere along the aircraft flight track. In situ measurements of O_3 were also made on the DC-8 to augment the lidar remote measurements and to provide a reference for correlating with the broad range of in situ gas and aerosol measurements also made on the DC-8. The flight tracks of the DC-8 in the western Pacific during TP are shown in Figure 1. A discussion of the TP science objectives, the characteristics of the instrumentation on the DC-8, and the DC-8 flight tracks over the entire Pacific Ocean are given in the overview paper by *Jacob et al.* [2003].

[4] Seventeen DC-8 science flights were made during TP with major bases of operations in Hong Kong, Yokota, Japan, and Hawaii. Local flights were performed from these locations, and long-range survey flights were conducted between these bases and on the out-bound and return flights between NASA Dryden Flight Research Center at Edwards Air Force Base, California, and Kona, Hawaii. Details about the flight objectives and the specifics of each flight are given in the overview paper [*Jacob et al.*, 2003]. The survey flights of the DC-8 consisted mainly of en route ascents and descents with short, typically less than 20 min, constant altitude legs at specific altitudes of interest that were identified using the remote sensing real-time lidar data. This allowed for extensive vertical sampling of the troposphere for chemical characterization along the flight track. On local flights the general strategy was to use the lidars to survey the troposphere along the flight track and to select the geographic regions and altitudes of interest for in situ airborne sampling. This approach allowed for the real-time synergistic use of data from the various sensors on the DC-8 to maximize the efficiency of the sampling strategy. This paper discusses the large-scale characteristics of the air masses observed on several TP flights in the western Pacific and their possible origins; the average latitudinal O_3 and aerosol distributions observed during TP and their relationship to various dynamical and chemical processes; the frequency of observation of different air mass types in different regions and altitudes; the average aerosol and chemical composition of these air mass types; comparison of these results with results made during PWB; the eastward flux of O_3 and its variation by latitude and altitude and air mass type during TP; and the eastward flux estimates for CO, CO_2, and CH_4.

2. Instrumentation and Methodology

[5] The NASA Langley Research Center's (LaRC) Airborne UV DIAL system has been described in detail in several previous publications [see e.g., *Richter et al.*, 1997; *Browell et al.*, 1998]. The LaRC Airborne DIAL system makes simultaneous measurements below and above the DC-8 for O_3 and multiwavelength aerosol backscatter measurements (576 and 1064 nm in nadir and 599 and 1064 nm in zenith) from near the surface to above the tropopause. The wavelength dependence of backscattering is derived from the visible (576/599 nm) and IR (1064 nm) measurements to provide information on the aerosol size distributions. In the nadir, simultaneous measurements of aerosol depolarization were also made at 576 nm for the detection of nonspherical aerosols, such as desert dust.

[6] The airborne DIAL system uses two 30-Hz, frequency-doubled Nd:YAG lasers to sequentially pump two dye lasers that are frequency-doubled into the UV to produce the online (288.2 nm) and off-line (299.6 nm) wavelengths for the DIAL O_3 measurements during TP. The residual 1064-nm and 576/599-nm beams from the frequency-doubling process of the Nd:YAG and dye lasers, respectively, are also transmitted with the UV DIAL wavelengths. As a result, four laser beams are transmitted simultaneously into the atmosphere below (288.2, 299.6, 576.4, and 1064 nm) and above (288.2, 299.6, 599.2, and 1064 nm) the aircraft for lidar measurements of O_3, aerosols, and clouds from near the surface to about 3 km above the tropopause. In addition to the normal lidar return detection at each of the laser wavelengths, the nadir 576.4-nm channel uses two separate detectors to determine the amount of depolarization introduced by aerosol scattering. This airborne DIAL system and the O_3, aerosol scattering ratio (ASR), and aerosol

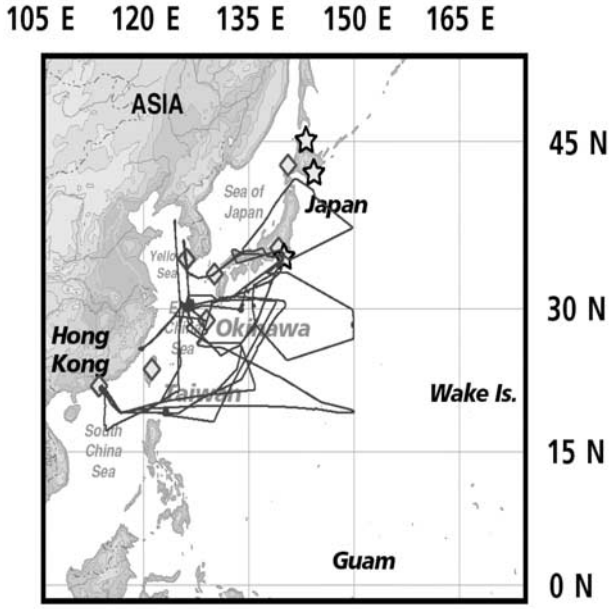

Figure 1. Flight tracks for NASA DC-8 aircraft in the western Pacific during TRACE-P. Ground-based remote gas measurements locations are indicated by stars and ozonesonde stations are indicated by diamonds.

depolarization (DPL) techniques have been used extensively in several recent tropospheric chemistry field experiments [see e.g., *Fenn et al.*, 1999; *Browell et al.*, 2001]. In addition, the wavelength dependence of aerosol backscattering (WVD) in this investigation was derived from a power law combination of the visible aerosol scattering ratio (ASR_{VS}) and the IR aerosol scattering ratio (ASR_{IR}) using the formulation presented by *Browell et al.* [1985] and subsequently used by *Sasano and Browell* [1989] to characterize the optical properties of different aerosol types.

[7] The UV DIAL system has an absolute accuracy for O_3 measurements of better than 10% or 2 ppbv (parts per billion by volume) and a measurement precision of 5% or 1 ppbv with a vertical resolution of 300 m and an averaging time of 5 min (about 70-km horizontal resolution at DC-8 ground speeds) [*Browell*, 1983; *Browell et al.*, 1983, 1985]. Intercomparisons between in situ and UV DIAL O_3 measurements were made throughout TP, and these results confirmed that the above measurement accuracy was being achieved, if not exceeded, during this field experiment.

[8] Since the UV DIAL remote O_3 profiles begin about 750 m above and below the aircraft, the O_3 distribution across this region is estimated by interpolating between the nadir and zenith UV DIAL measurements with the in situ O_3 measurement used to constrain the interpolation in between. Ozone distributions were also extrapolated from the lowest UV DIAL measurement altitude (usually below 1 km) to the surface using the gradient in O_3 concentrations determined from the in situ measurements. These techniques were previously discussed for the UV DIAL O_3 distributions from the PEM Tropics A [*Fenn et al.*, 1999] and PEM Tropics B [*Browell et al.*, 2001] field experiments.

[9] Meteorological analyses of the potential vorticity (PV) distributions along the flight track were used to indicate the fraction of observed O_3 that could be attributed to stratosphere-troposphere exchange (STE) using an O_3 to PV ratio derived in the lower stratosphere. This method has been previously used by *Browell et al.* [1996a, 2001] and *Fenn et al.* [1999] in a number of previous tropospheric O_3 studies. The specific O_3 to PV ratio used in the current air mass characterization analysis for TP is discussed in section 4.

[10] Five-day backward trajectories are also used to indicate the possible origin of observed air masses. These backward trajectories were calculated using the Florida State University (FSU) kinematic backward trajectory model. Air parcels along the flight track were selected at specific pressure altitudes, and these air parcels were followed back to their origins five days earlier (unless the trajectory terminates early at the surface). The consistency of the backward trajectories can be tested by using an ensemble of air parcels. This approach is discussed by *Fuelberg et al.* [2003]. The backward trajectories shown in this paper are used to describe the general characteristics of the air mass's source region.

3. Results and Discussion

3.1. Air Masses Observed Over the Western Pacific

[11] An example of the resulting O_3 and aerosol distributions observed during TP is shown in Figure 2 (note that all of the UV DIAL data are posted at our web site at http://asd-www.larc.nasa.gov/lidar/). The data were obtained on a long-range survey flight from Guam to Hong Kong on 3–4 March 2001, and the large-scale variations of O_3, ASR_{VS}, WVD, and DPL are shown for this flight. The flight track is shown superimposed on a GOES-8 visible satellite image, and the aircraft flight altitude can be seen as a black line in the aerosol cross sections. A low-level front was crossed at about 0300 UT at 22°N/134°E, and most of the clouds seen in the GOES-8 image are near the surface and readily seen in the ASR_{VS} data. The tops of the optically thick clouds can be readily seen in the lidar data because they have a white (data void) region on the other side of the highly scattering cloud top region. Optically thin clouds exhibit an ASR_{VS} that exceeds 5, but they are not so highly attenuating that a measurement cannot be made on the other side of it, although there may be some underestimation of the scattering from the other side due to that attenuation. This is true for both optically thin low-level clouds as well as cirrus clouds in the middle to upper troposphere.

[12] The location of the low-level front coincides with an abrupt change in O_3 levels at the frontal location. The O_3 levels SE of the front were generally <30 ppbv, which is indicative of the clean marine lower-troposphere over the Pacific; while NW of the front, O_3 was generally >40 ppbv with some regions up to 70 ppbv, which is impacted significantly by direct outflow from Asia behind the front. The characteristics of the aerosols also changed dramatically across the front. The ASR_{VS} above the marine boundary layer (MBL) increased abruptly in the Asian outflow NW of the front, and the WVD and DPL data showed that there was an increase in large (low WVD), depolarizing (nonspherical) aerosols that were present in the outflow below about 4–5 km. This was particularly true in general north of 19°N with enhanced depolarization all the way to the surface at the northernmost point. The low-level 5-day backward trajectories (not shown) indicated that north

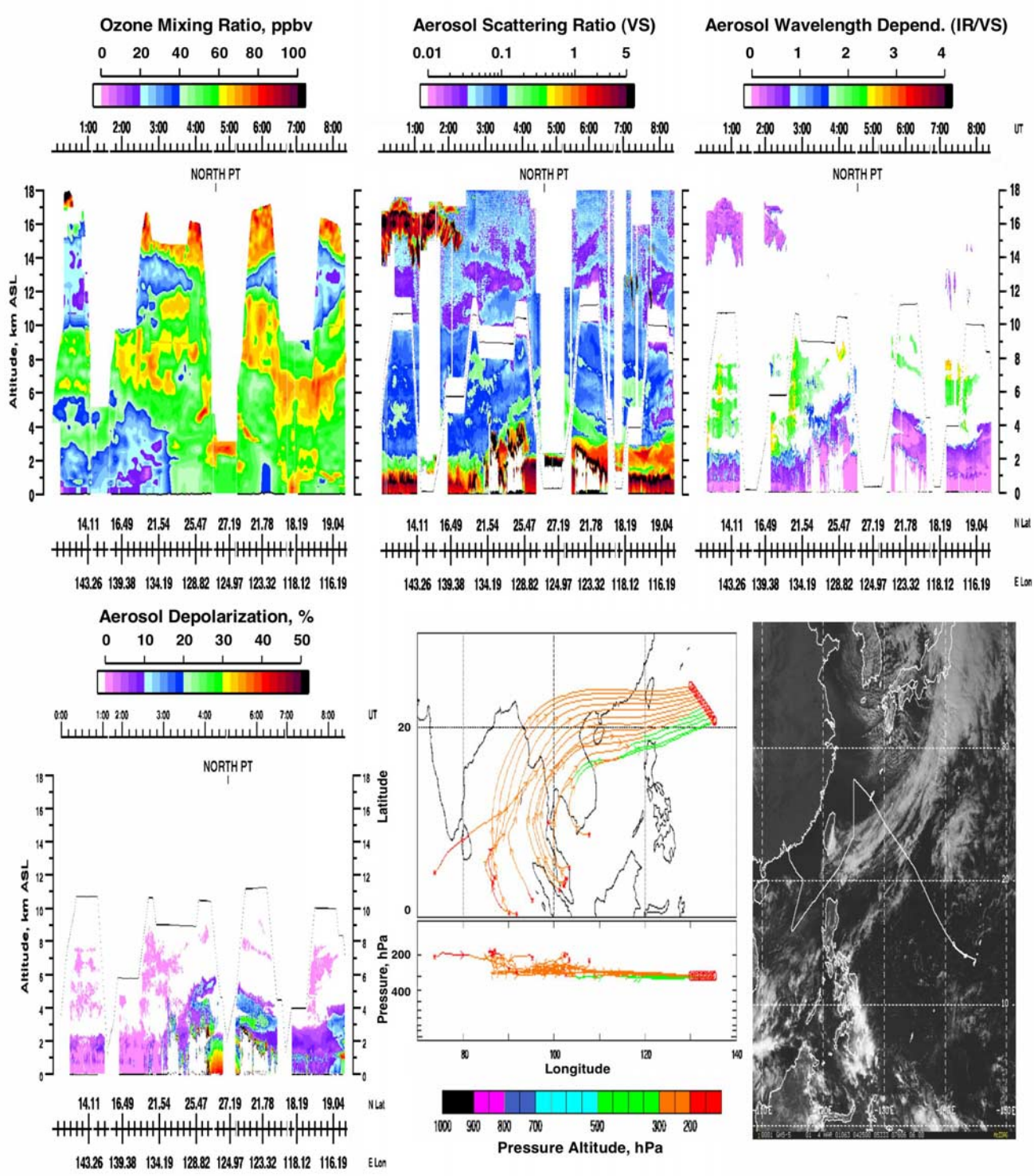

Figure 2. Ozone (top left), aerosol scattering ratio (top center), aerosol backscatter wavelength dependence (top right), and aerosol depolarization distributions (bottom left) observed on flight from Guam to Hong Kong on 4 March 2001 (Flight 6). Also shown are 5-day backward trajectories that end at 300 hPa on a portion of the flight track and a GOES-8 visible satellite image with flight track superimposed. The aircraft flight altitude is shown on the aerosol plots as a continuous black line. In situ O_3 measurements were used to constrain and interpolate the O_3 data across the DIAL measurement gap near the aircraft.

of about 20°N the Asian outflow could be a mixture of continental pollution and desert aerosols with the effect being stronger with increasing latitude. This situation was found to be common in the low-level Asian outflow during TP.

[13] In the midtroposphere (5–10 km), the air mass observed during this flight was more homogeneous and showed little influence from the low-level front. The O_3 levels were in the 50–70 ppbv range, which is significantly

enhanced over the clean marine O_3 levels, and the aerosols had low ASR_{VS} (<0.15), low DPL (<1 %), and enhanced WVD (2–2.5), which indicates small, spherical aerosols with low aerosol number densities. The 5-day backward trajectories are also shown in Figure 2 for air ending at 300 hPa (~8-km altitude) along the flight track. These backward trajectories show that the air came from the region of SE Asia where biomass burning was occurring [*Heald et al.*, 2003; *Liu et al.*, 2003], and the air only slightly descended during the advection to the measurement region. Convective transport into the middle to upper troposphere of air from biomass burning is consistent with the observation of photochemically produced O_3 and the presence of small aerosols that are left when the air goes through the cloud convection process. These characteristics of air from biomass burning in the midtroposphere were frequently found during TP, which will be discussed more in section 3.

[14] The low-O_3 regions in the upper troposphere resulted from convective pumping of low-O_3 air from near the surface in the tropics. This was a common feature observed in the western Pacific during PWA [*Browell et al.*, 1996a] and PWB [*Fenn et al.*, 1997; *Browell et al.*, 1998]. Cirrus clouds, which also can result from this same convection, can be seen above 14 km before 2:20 UT, and they had enhanced ASR_{VS} (>2) and low WVD (~0), which is indicative of subvisible cirrus clouds containing large ice particles.

[15] An example of the outflow of continental pollution was observed on the flight from Okinawa to Hong Kong on 10 March 2001, which had a long-flight leg over the Yellow Sea. Figure 3 shows the O_3 and ASR_{IR} obtained on this flight. Elevated levels of O_3 and ASR_{IR} were found below ~4 km over the entire region from 20 to 37°N. The pollution was flowing easterly from China at all altitudes in the lower troposphere. Backward trajectories, ending at 500 hPa over the Yellow Sea, are shown in Figure 3, and some of them start near the surface in the western Mediterranean region. It is clear that there are many sources of aerosols and O_3 that have contributed to the observed high level of pollution that was observed in the low to middle troposphere in this region. Noncloud ASR_{IR} levels of >10 were observed in the lower troposphere over the Yellow Sea with only moderate levels of O_3 (60–70 ppbv), which is attributed to more recent emissions of pollutants from coastal regions of China. The GOES visible image in Figure 3 shows the band of clouds that were crossed from ~30 to 22°N on the southerly flight leg, and these optically thick clouds can be seen in the ASR_{IR} data with tops decreasing in altitude from 12 to 6 km, respectively. Above the clouds and in the lower aerosol loaded region above ~6 km and north of 32°N, the elevated O_3 is generally correlated with enhanced PV associated with a stratospheric intrusion and a low tropopause (~9.5 km) near the northernmost point at ~37°N. The downward sloping tropopause to the north is reflected in the O_3 data above 14 km. Based on the backward trajectories, the low O_3 and aerosol levels south of ~22°N and below ~8 km are associated with clean marine air, and the O_3 maximum near 10 km in this region was from a biomass burning source in SE Asia. This biomass burning feature is similar to that previously discussed for the flight from Guam to Hong Kong on 3–4 March 2001 (Figure 2).

[16] Cross sectional data were obtained on O_3, ASR_{IR}, ASR_{VS}, WVD, and DPL on each flight during TP, and when coupled with backward trajectory and PV analyses, they showed a wide range of atmospheric conditions and processes that contributed to producing the large-scale distribution of O_3 and aerosols over the western Pacific. The O_3 cross sections from each flight were used extensively to evaluate the predictive capability of chemical transport models, and it was found that these models can reasonably simulate the regional tropospheric O_3 distribution in the free troposphere [*Pierce et al.*, 2003; *Wild et al.*, 2003]. The following section addresses the large-scale average distributions of O_3 and aerosols observed during TP and compares them to what was observed during PWB.

3.2. Average Distributions and Air Mass Characteristics

[17] To derive the average latitudinal and longitudinal O_3 and aerosol distributions observed during TP, each individual flight was initially averaged into a latitudinal/longitudinal cross section with bins of 30 m in the vertical and 0.25° of latitude or 0.5° of longitude in the horizontal. This method is discussed in more detail by *Browell et al.* [1996b]. To eliminate biasing of the average background aerosol cross sections by clouds, a cloud detection technique was used with a nominal cloud threshold of $ASR_{VS} > 10$ in the low to middle troposphere and >0.5 in the upper troposphere (slightly variations in criteria were needed on some flights). Aerosol data within 90 m of a cloud were omitted from the average as were potentially attenuated aerosol data on the far side of a cloud. This approach was first used by *Browell et al.* [2003] to investigate the springtime trend in aerosols during the Tropospheric Ozone Production about the Spring Equinox (TOPSE) field experiment in 2000.

[18] The average latitudinal/longitudinal distributions from all the flights were equally weighted and averaged together to arrive at the overall average latitudinal/longitudinal distribution for the campaign. Calculations of the average latitudinal distributions were limited to the western Pacific region (<150°E), and the average longitudinal distributions were separately calculated for the 10–20°N, 20–30°N, and 30–50°N latitude regions.

[19] The average latitudinal O_3 and ASR_{VS} distributions in the western Pacific are shown in Figure 4. The full altitude range of the O_3 and ASR_{VS} data was used to produce the distribution on the left of Figure 4 (All). The O_3 distribution clearly shows the latitudinal variation in the tropopause height from 17 km at 20°N to 8.5 km at 46°N with an abrupt decrease in height near 30°N, which corresponds to the vicinity of the subtropical jet. The irregular structure in the average O_3 data north of 30°N is associated with the variability in the stratospheric intrusions, which are very frequently observed in this region. Some of the intrusions extend into the troposphere as can be readily seen in the O_3 cross section. The average ASR_{VS} above the tropopause is near the background levels for these aerosol measurements (<0.05). In order to get a better indication of the variability of tropospheric O_3 and aerosols, the cross sections of O_3 for the individual flights were used to define the tropopause level, either by using the gradient technique, as previously described by *Browell et al.* [1996b] or the 100-ppbv level if there were not enough data to use the gradient technique. To avoid biasing of the average tropospheric O_3 and aerosol cross sections for each flight, all O_3

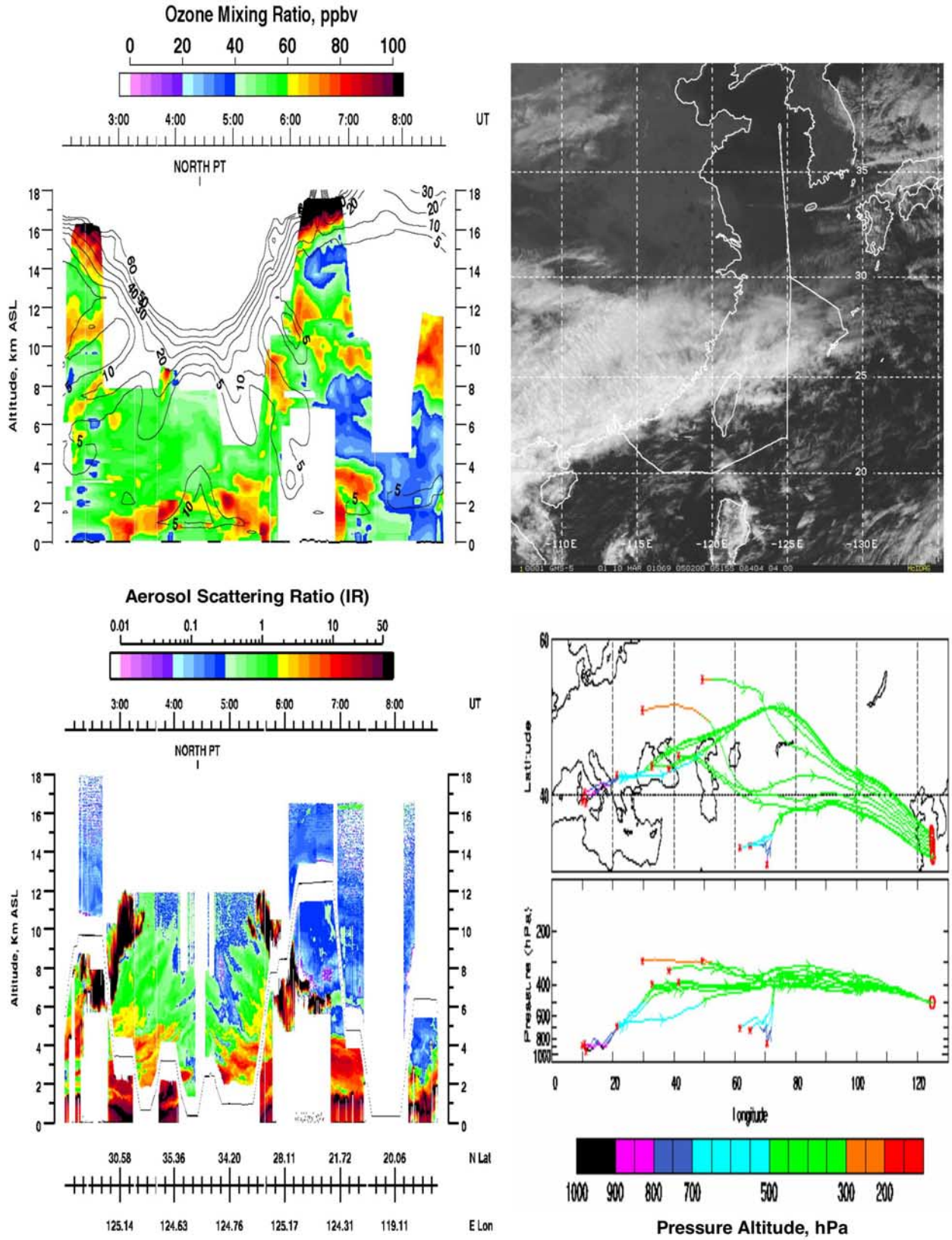

Figure 3. Ozone with PV isopleths (≤60 PVU) (top left) and IR aerosol scattering ratios (bottom left) observed on flight from Okinawa to Yellow Sea to Hong Kong on 10 March 2001 (Flight 9). Also shown are the GOES-8 visible satellite image with flight track superimposed (upper right) and 5-day backward trajectories that end at 500 hPa on the Yellow Sea portion of the flight track (lower right).

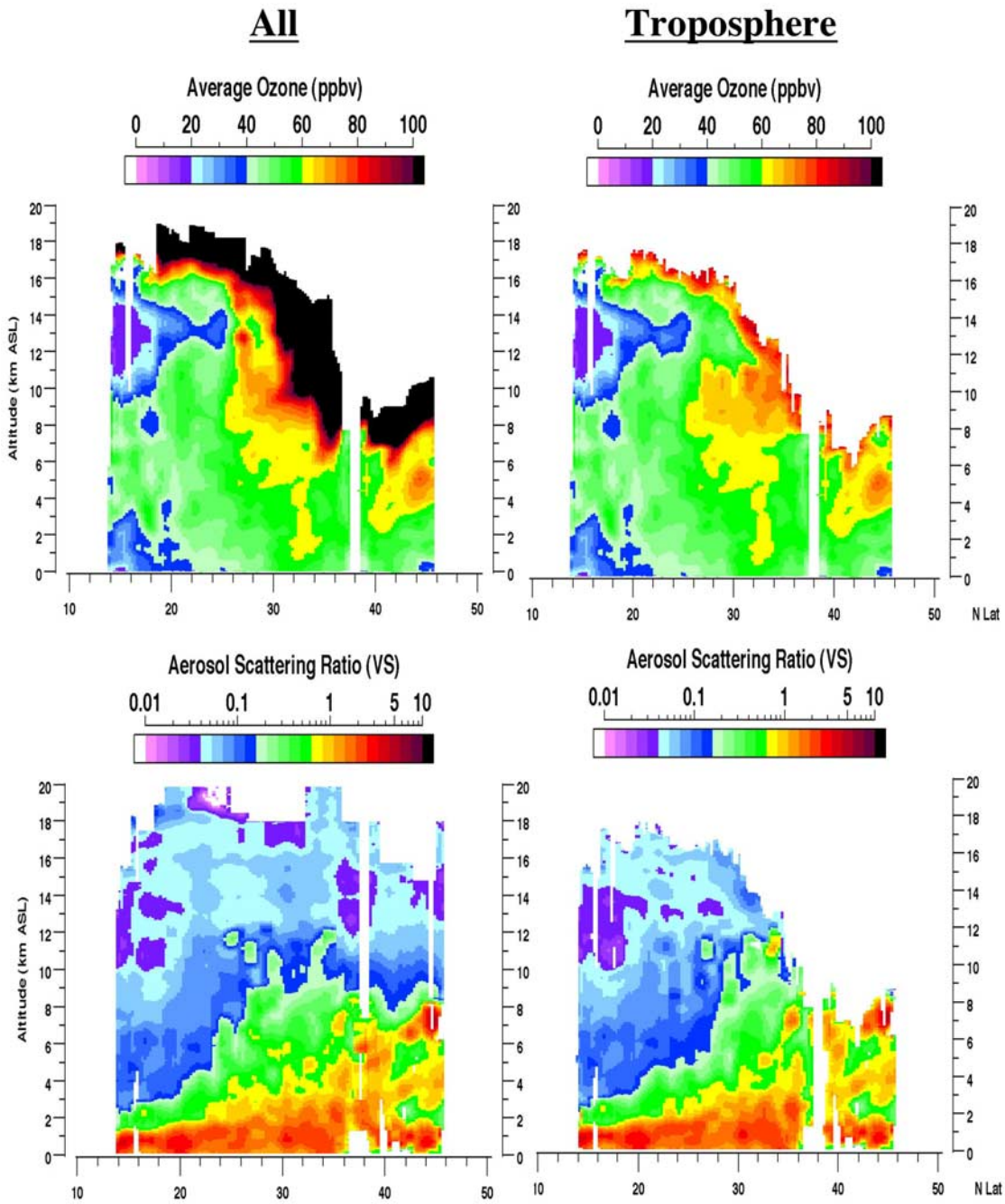

Figure 4. Average latitudinal O_3 (top) and aerosol (bottom) distributions observed during TRACE-P over the western Pacific (west of 150°E). Left panels include all data (tropospheric and stratospheric) and right panels include only tropospheric data.

and ASR data were excluded within 1 km of the tropopause or where O_3 exceeds 100 ppbv. The aerosol data were also limited to the same altitude range as defined by the tropospheric O_3 data. The resulting average tropospheric O_3 and ASR_{VS} distributions are shown beside the combined distributions in Figure 4.

[20] The above analysis technique removes the O_3 above the tropopause and the high O_3 in the direct intrusion events, but an enhancement in O_3 just below the tropopause is clearly evident in the average cross section. A major enhancement in O_3 can also be seen in the midtroposphere (8–10 km) from 25–34°N, which is in the vicinity of where the major intrusions were occurring. The general characteristics of the O_3 distribution reflects the O_3 destruction near the surface (<2 km) in the tropics (<20°N) [*Thompson et al.*, 1993]; convection of low-O_3 surface air into the upper troposphere [*Pickering et al.*, 2001]; transport of O_3 from subtropics and midlatitudes into the tropics in the midtroposphere; and various sources of enhanced O_3 (stratospheric and photochemical) throughout the troposphere north of 20°N. In the 0–8-km range from 25 to 46°N, the median O_3 value was found to be 58.1 ppbv. The aerosol distribution shows an

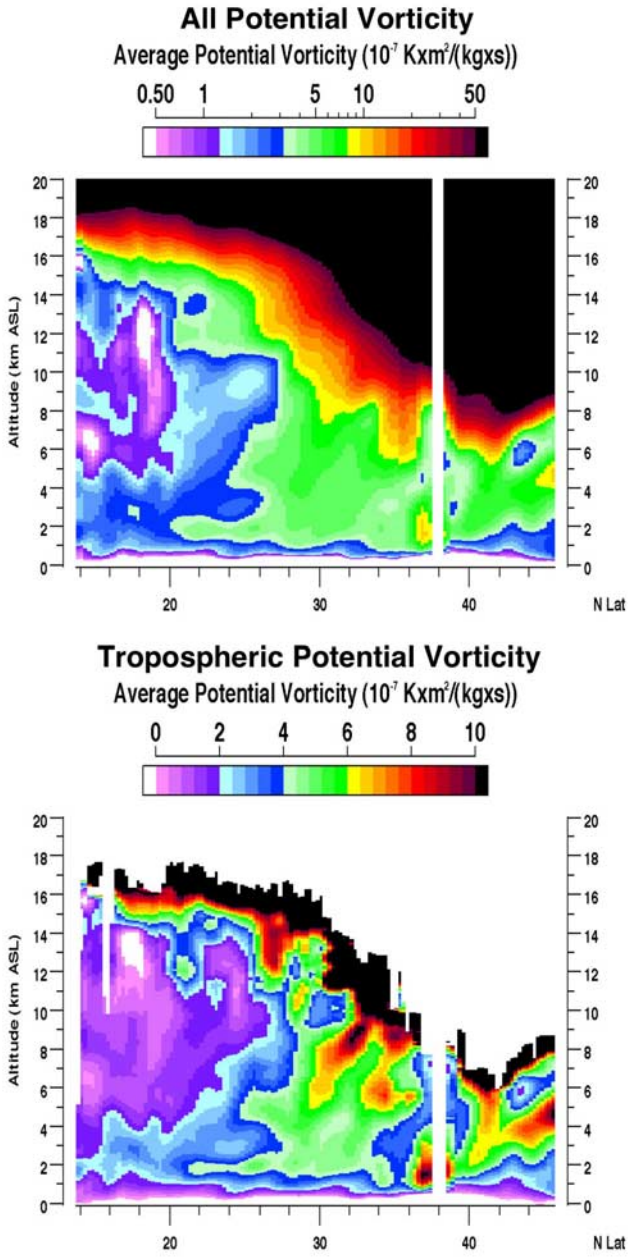

Figure 5. Average total (top) and tropospheric (bottom) latitudinal potential vorticity distributions obtained during TRACE-P.

increasing influence of continental sources with latitude up to about 45°N. Since the stratospheric aerosol loading is low compared to tropospheric levels, as can be seen by comparing the two aerosol figures in Figure 4, the increase in aerosols with increasing latitude is primarily due to easterly advection of continental pollution, which includes dust aerosols [*Murayama et al.*, 2001; *Wang et al.*, 2000; *Sun et al.*, 2001; *Pierce et al.*, 2003]. The median value of ASR_{VS} in the 0–8-km, 25–46°N region was found to be 0.74. The low aerosol loading in the upper troposphere south of 30°N is associated with the removal of aerosols by cirrus clouds.

[21] The average latitudinal PV distribution was derived using the same approach described above, and the results are shown in Figure 5. The average total PV cross section exhibits the same general features in the tropopause behavior that was observed in the average O_3 cross section shown in Figure 4. The locations of the major intrusions are well represented in the PV distribution north of 26°N. The PV distributions were masked using the tropospheric O_3 data as discussed above, and the result is shown in the lower panel of Figure 5. The region of high residual PV below the tropopause corresponds to the region of enhanced O_3 shown in Figure 4 (upper right panel). This is a strong indication that most of this O_3 is of stratospheric origin as might be expected this close to the tropopause. There are a considerable number of enhanced PV levels (PVU > 4, which represents O_3 levels >25 ppbv (to be discussed later)) throughout most of the troposphere north of 26°N. At the same time, this is the region which has considerable aerosol loading (ASR_{VS} > 0.5) and enhanced O_3 (>55 ppbv). One region that has enhanced O_3 in it with no enhanced PV is the region in the midtroposphere (6–11 km) south of 28°N with the region expanding to 2–12 km near 25°N. This is the region where the biomass burning emissions were predominantly observed [*Heald et al.*, 2003] as mentioned in the discussion of Figures 2 and 3. Based on O_3, aerosols, and PV distributions, the troposphere north of 26°N is a complex mixture of STE, pollution advection, and photochemical processes.

[22] PWB was conducted about 3 weeks earlier in the same season, and the average tropospheric latitudinal O_3 and ASR_{VS} distributions observed for this experiment are presented in Figure 6. The same criteria and methodology were used for deriving these distributions as for the TP cross sections shown in Figure 4. As can be seen in the figure, the latitude coverage for PWB in the western Pacific (10°S–57°N) was much larger than for TP (14–46°N). As a result, the low-O_3 region near the surface and in the upper troposphere in the tropics is even better characterized than what can be seen in the TP O_3 data. The O_3 loss in the Southern Hemispheric (SH) air near the surface and its transport through deep convection into the upper troposphere has been previously discussed by *Browell et al.* [2001], and it is graphically represented in the average O_3 distribution shown in Figure 6. The enhanced O_3 just below the tropopause is seen in the PWB data as it was for TP, although the amount of enhanced O_3 in the vicinity of the intrusions appears to be less during PWB. The O_3 distribution in PWB across the troposphere was remarkably uniform (40–60 ppbv) below about 8 km from 16 to 52°N with a median of 48.9 ppbv in the 25–46°N region. The average aerosol loading increased in the free troposphere north of about 20°N, as it did for TP, and ASR_{VS} had a median value of 0.36 in the 0–8-km, 25–46°N region.

[23] The average O_3 and ASR_{VS} levels for TP were higher than that observed during PWB, and Figure 7 shows the cross sectional differences between the two campaigns (TP-PWB). In the lower troposphere south of about 25°N, O_3 in TP was slightly less than in PWB. Nearly everywhere else, the TP O_3 was higher than in PWB. Over the entire cross section the O_3 increased by a median value of 7.1 ppbv. In the region north of 25°N, the O_3 median increase was 9.9 ppbv, which represents a 20% increase in O_3 from a PWB value of 49.1 ppbv. Below 8 km in the same latitude range, the median O_3 increase was 9.4 ppbv (19%). The difference in the ASR_{VS} distributions is also

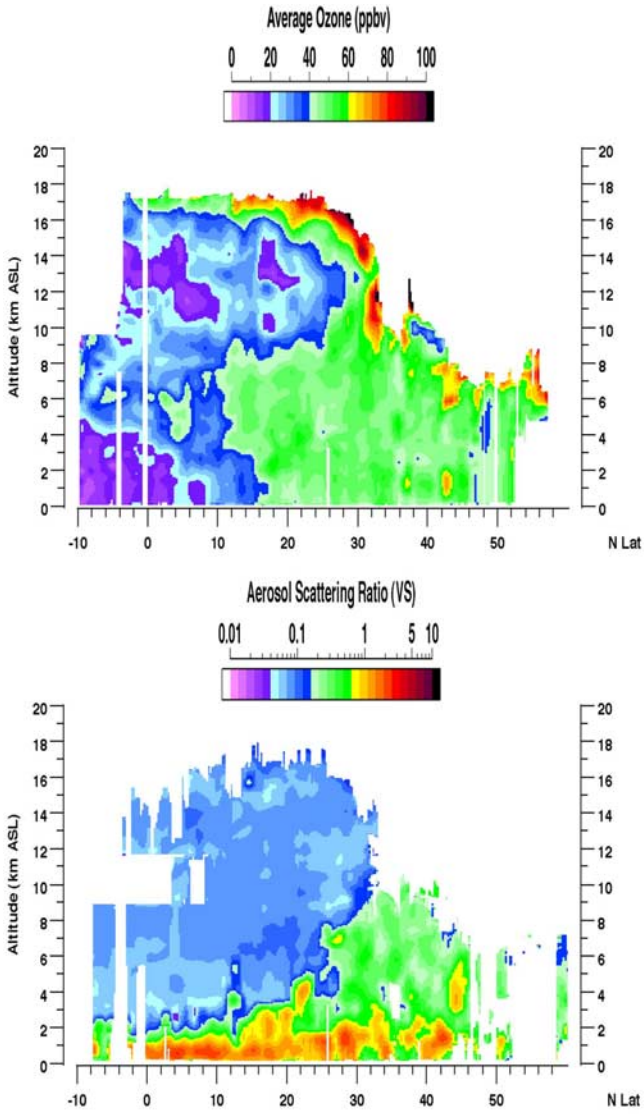

Figure 6. Average latitudinal tropospheric ozone (top) and aerosol scattering ratio (bottom) distributions observed during PEM West-B over the western Pacific (west of 150°E).

shown in Figure 7, and it shows that most of the increase in the TP aerosol loading was in the 0–8-km, 25–46°N region with a median ASR_{VS} increase of 0.28, which is a 78% increase over the PWB value.

[24] To provide insight into the possible changes associated with STE between TP and PWB, the average latitudinal PV distribution for PWB was calculated and subtracted from the average PV distribution for TP (Figure 5), and the result is shown in Figure 7. There is a general increase in PV nearly everywhere except in the middle to upper troposphere in the tropics and in the regions of large negative PV differences near 10 km at 31°N and near 6 km at 44°N. These features result from PV analyses in the vicinity of several intrusions during PWB that did not spatially coincide with the observed intrusions. The spatial inconsistency between the PV analysis and the O_3 observations results in a residual artifact of high PV that can get into the average PV cross section. The overall increase in PV between the two campaigns is clearly evident. To estimate the amount of O_3 associated with STE and the PV difference, we use an assumed O_3 to PV ratio of 6.4 ppbv/PVU (to be discussed in next section) to convert the PV difference plot to a stratospheric equivalent O_3 distribution using a different scale in Figure 7. The median value for the equivalent O_3 increase was found to be 5.6 ppbv for the entire cross section and 10.4 ppbv for the 0–8-km, 25–46°N region. This indicates that a significant portion of the difference in the O_3 levels between the two campaigns may be due to increased STE in TP compared to PWB, and this may be associated with the slightly later time frame for the TP campaign, which is also associated with increased STE activity into the springtime.

[25] The average longitudinal O_3 and aerosol cross sections in different latitude regions are shown in Figure 8. Gaps in the data represent regions where there were either no flights or an altitude range that was not covered with any measurements in the flights that were made. In the tropics (10–20°N), the general trends in O_3 and aerosols were similar to those previously mentioned in the tropical western Pacific (west of 150°E). The region of low O_3 and low aerosol scattering in the upper troposphere were significantly deeper in the 150–190°E region covering the entire 5–16-km region near 180°E. In the lower troposphere east of 165°E a layer was observed centered at ~3 km with significantly enhanced O_3 and aerosols. This layer appeared to be contiguous with a deep layer of O_3 and aerosols covering most of the troposphere near 200°E. Backward trajectories showed that this air was transported from Asia across the northern Pacific, around a high-pressure system, and into the tropics. This is an entirely different transport regime than the more direct eastward transport of biomass burning air which is responsible for the midtropospheric enhanced O_3 and aerosols in the western Pacific.

[26] In the subtropical region (20–30°N), the general nature of the O_3 and aerosol distribution is very different between west of 145°E and east of 178°E. West of 145°E, the O_3 distribution was more uniform across the troposphere with a slight increase in O_3 across the midtroposphere. The aerosols were mostly below about 5 km with very low aerosol loading in the upper troposphere. East of 145°E, and more particularly, east of 178°E (due to a large data gap), there was enhanced O_3 and aerosols across nearly the entire troposphere. This was due to the outflow from Asia that occurs to the north of this region and then is transported equatorward around a climatological anticyclonic feature in the western Pacific [*Fuelberg et al.*, 2003]. This type of long-range transport of Asian aerosols to Hawaii has been previously reported by *Perry et al.* [1999]. While the aerosols observed in TP indicate a continental source, some of the enhanced O_3 could also be from STE activity north of 30°N, which is where most of the STE was observed to be occurring in the western Pacific (see Figures 4 and 5). In the 30–50°N midlatitude region, O_3 is enhanced across all of the troposphere at all longitudes; however, there appears to be more O_3 in the lower troposphere below 5 km west of 180°E than in the eastern Pacific (east of about 210°E). There is significant aerosol loading throughout the low to middle troposphere in the western Pacific, which is associated with the eastward advection of continental pollution and dust, particularly behind fronts. While the aerosol loading was found to generally decrease in the free troposphere to the east

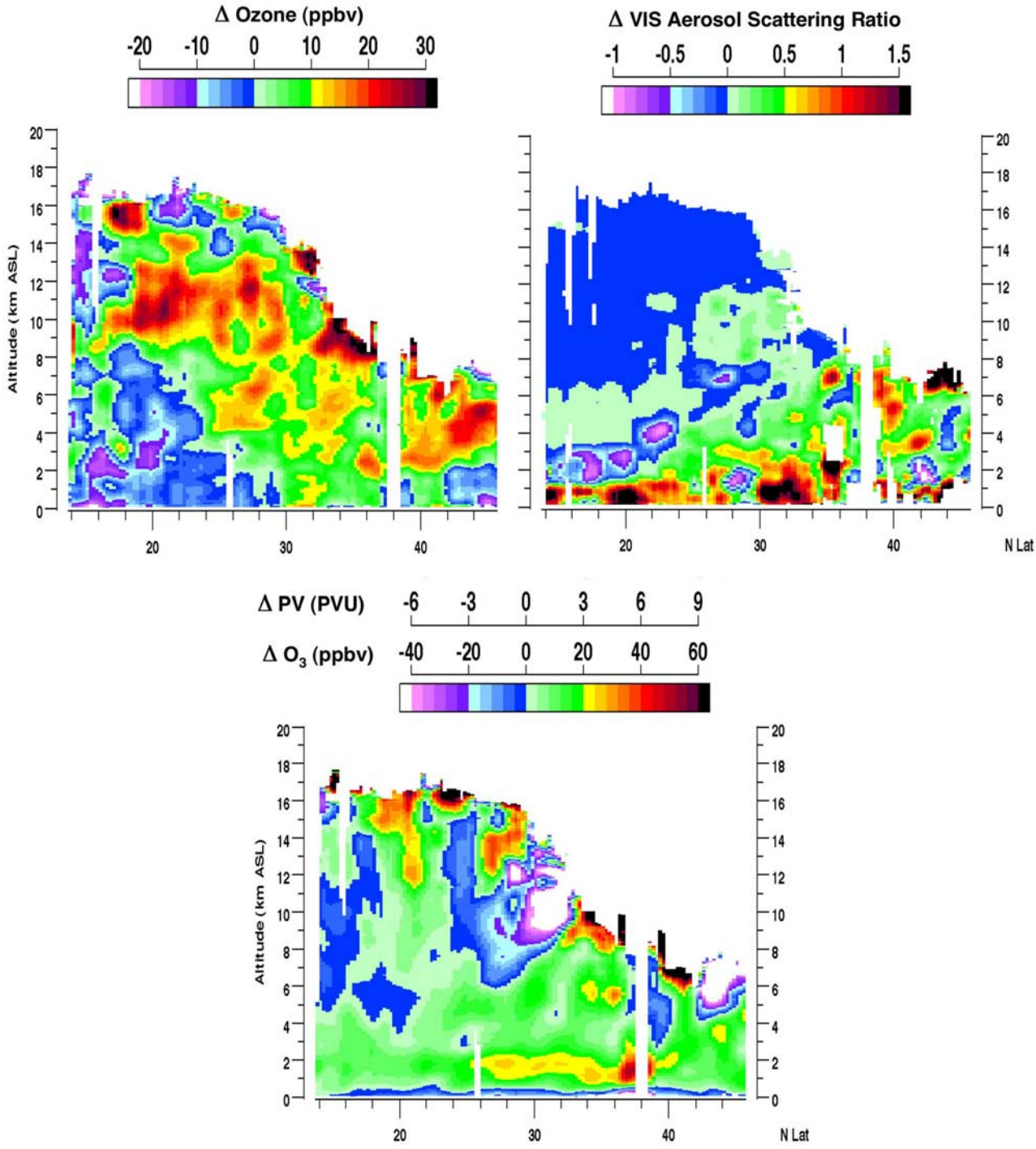

Figure 7. Change in average latitudinal tropospheric O_3 (top left), aerosol (top right), potential vorticity(PV) and PV equivalent O3 (based on ratio of 6.4 ppbv/PVU) (right) distributions observed over the western Pacific (west of 150°E) from PEM West-B to TRACE-P. Differences are given only for common measurement regions.

of 150°E, there was still significant aerosol loading observed across the entire Pacific in this latitude band.

3.3. Air Mass Characterization

3.3.1. Air Mass Types and Observations

[27] Based on O_3, ASR_{VS}, and PV levels observed on each TP flight, air mass types were identified and quantified based on the fraction of the time they were observed in different regions over the Pacific as a function of altitude. This approach has been used on several previous tropospheric field experiments over the Pacific [*Browell et al.*, 1996a, 2001; *Fenn et al.*, 1997, 1999]. In this method, an O_3 profile is designed to allow for the discrimination of different types of air masses that have localized variations

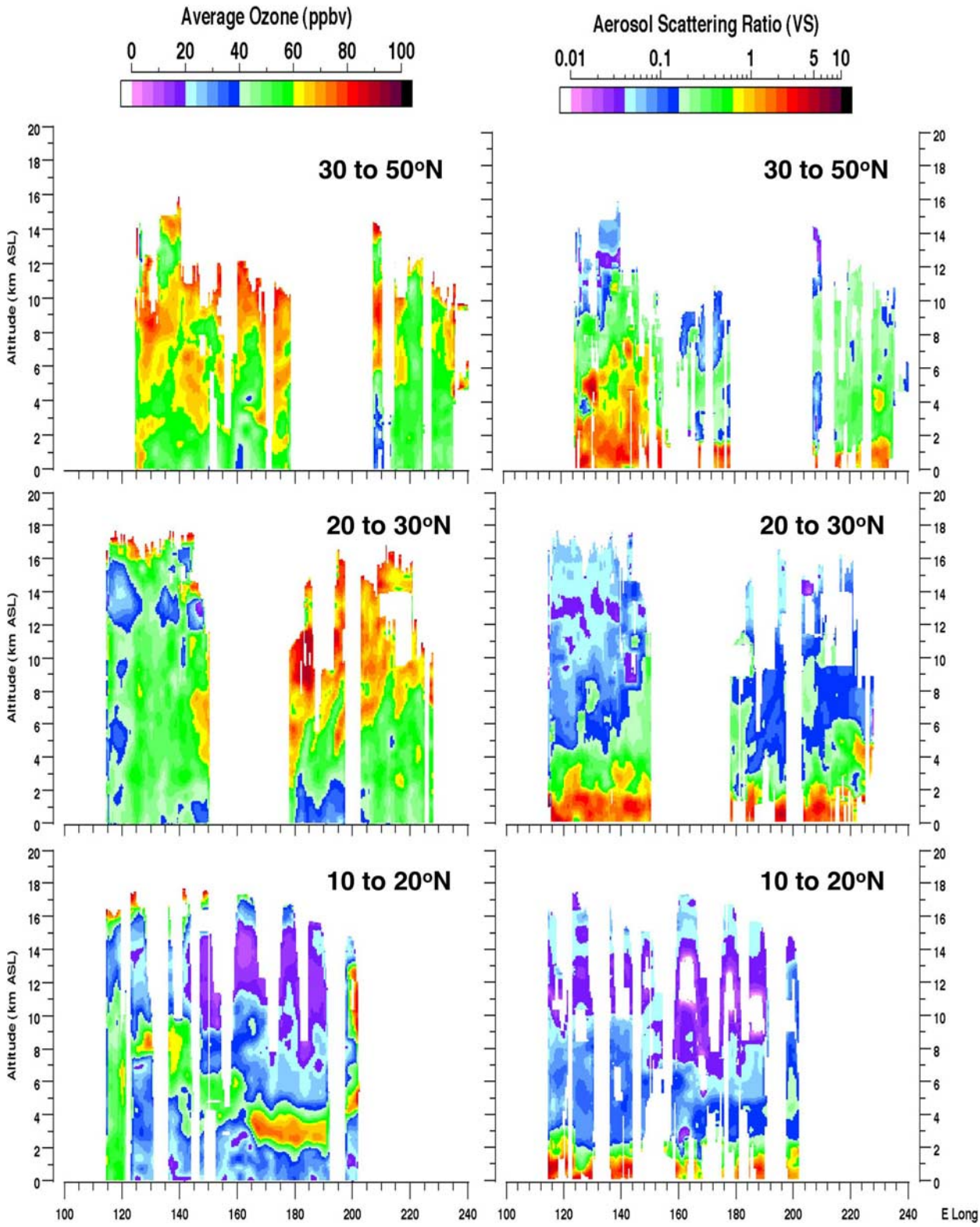

Figure 8. Average longitudinal tropospheric ozone (left) and aerosol (right) distributions observed during TRACE-P over the western Pacific in the latitudinal regions shown.

due to recent source and sink processes. The reference O_3 profile used for TP (and PWB) is shown in Figure 9. Above 5 km, this profile is the same as was used in the PWA air mass characterization [*Browell et al.*, 1996a], but from 5 km to the surface, the TP profile decreases linearly to 33 ppbv, whereas for PWA the profile decreased linearly to 12 ppbv due to the predominance of much cleaner, low-O_3 marine air that was observed in the westerly flow over the western Pacific during the summertime [*Browell et al.*, 1996a]. In addition to the O_3 reference profile, the amount of aerosol loading as defined by the ASR_{VS} was also used to discriminate between air with low aerosol loading (defined as $ASR_{VS} < 0.1$), and air with enhanced aerosol loading such as in plumes. Potential vorticity cross sections derived from ECMWF meteorological analyses were used to further categorize the air mass types when the O_3 was sufficiently enhanced over the reference O_3 profile. In order to quantify the amount of O_3 from the stratosphere that would have been recently transported with the PV into the troposphere via STE, the relationship between O_3 and PV in the lower stratospheric air had to be determined. In situ O_3 measurements and the PV analyses from TP and PWB were used for all clearly defined stratospheric cases for PV $\geq$ 10, and those results are plotted in Figure 9 along with the linear best fit to the data, which is constrained to pass through the origin. The slope of the best-fit line is 6.4 ppbv/PVU, and this relationship was used to estimate the amount of stratospheric air that was present in an observed air mass. This approach has been used to examine the contribution of STE to investigations of the tropospheric O_3 budget in the tropics [*Fenn et al.*, 1999; *Browell et al.*, 2001] and the springtime O_3 trend in the Arctic [*Browell et al.*, 2003].

[28] The criteria for categorizing the different air mass types are given in Table 1. Nine of the 11 air mass categories have been used previously in tropical O_3 studies [*Fenn et al.*, 1999; *Browell et al.*, 2001]. The enhanced O_3 and enhanced aerosol category, previously designated as HPLU, has been further subclassified using the amount of PV-derived equivalent O_3 in the observed air mass. This was necessary since it was found during TP that there were many cases when air with enhanced O_3 (>20% above reference O_3 profile) and enhanced aerosol loading (ASR_{VS} >0.1) also exhibited significant levels of PV (>60% of observed O_3 attributed to stratosphere in some cases). This mixture of continental pollution with stratospheric air had to be accounted for in the air mass characterization. As a result, the previously defined category of HPLU was subcategorized into HPLU, HPLM, and HPLV based on the relative fraction of stratospheric-derived O_3 in the air mass. This is similar to the subcategorization that had previously been put into place for air masses with enhanced O_3, low aerosol loading, and varying amounts of stratospheric-derived O_3 (HO3, HO3M, and SINF). The specific criteria used for each air mass category are given in Table 1, and except for the new categories mentioned above, the air mass categories have been previously discussed in detail by *Browell et al.* [1996a, 2001] and *Fenn et al.* [1999].

[29] An example of the air mass categorization applied to the data from a TP flight is shown in Figure 10. The O_3, ASR_{VS}, and PV distributions and the resulting air mass types are shown for the flight from Hong Kong to Okinawa on 17 March 2001. A large region with elevated PV, O_3, and

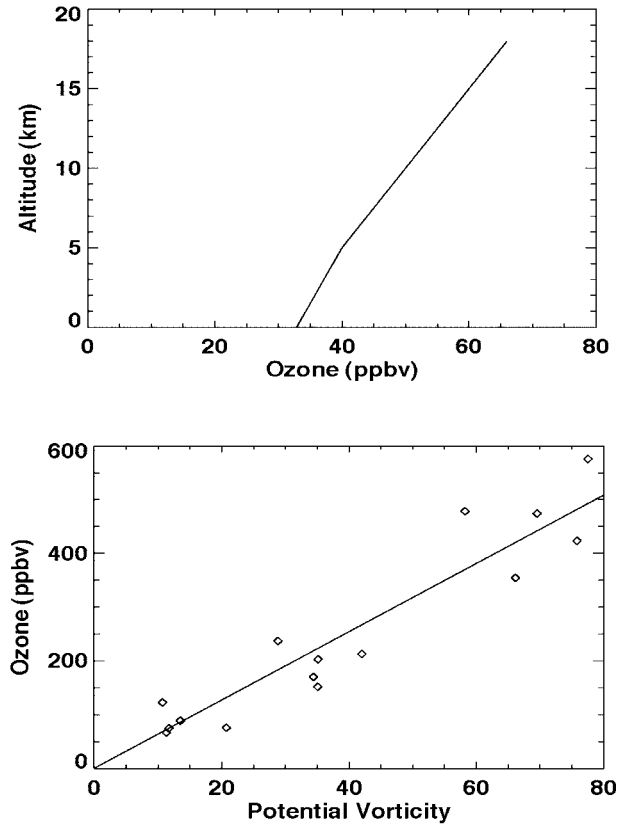

Figure 9. Ozone discriminator (top) used in air mass characterization for TRACE-P and PEM West-B and ozone and PV data (bottom) from TRACE-P and PEM West-B in situ measurements and ECMWF meteorological analysis that were used to determine the ozone to PV relationship in lower stratosphere of 6.4 ppbv/PVU.

aerosol loading can be seen centered at about 6 km and 0700 UT, and this is categorized as HPLV due to this unique combination of parameters. This is clearly a mixture of continental pollution and stratospheric air, which results from upstream mixing of air masses. This could happen in the upper troposphere when pollutants get transported upward due to convection or frontal lifting and then mixed with stratospheric air coming into the troposphere in an intrusion (see also M. A. Avery et al., Complex composition of the upper troposphere in the vicinity of the Japan Jet observed during the TRACE-P mission, submitted to *Journal of Geophysical Research*, 2003, hereinafter referred to as Avery et al., submitted manuscript, 2003). Also, the rapid advection of air in an intrusion in the middle to lower troposphere can mix in with continental pollution, including desert dust, and carry the mixture out over the Pacific in a common air mass. The backward trajectories for the HPLV air mass support the second hypothesis for the generation of this air mass mixture. The predominant stratospheric air mass type (SINF) was identified adjacent to the HPLV air and in the upper troposphere, just below the tropopause. There are other regions in the midtroposphere that have enhanced O_3 associated with them and no appreciable aerosol enhancement and no elevated PV, and these air masses are categorized as HO3, where the O_3 is thought to be of photochemical origin. The low-O_3

Table 1. Air Mass Types

Air Mass Type	Definition
Reference (REF)	O_3 within 20% of O_3 reference profile (RP) and low ASR_{VS} (<0.1).
Near Surface (NS)	Air with high aerosol loading ($ASR_{VS} > 0.5$) associated with boundary layer.
Background Ozone Plume (BPLU)	O_3 within 20% of RP and $ASR_{VS} > 0.1$.
Convective Outflow/Clean Pacific (CON/CP)	$O_3 > 20\%$ below RP and with/without cirrus clouds in vicinity.
Low Ozone Plume (LPLU)	$O_3 > 20\%$ below RP and $ASR_{VS} > 0.1$.
High Ozone Plume (HPLU)	$O_3 > 20\%$ above RP, $ASR_{VS} > 0.1$, and less than 25% of O_3 estimated from stratosphere based on PV and assumed O_3/PV relationship.
High Ozone Plume-Mixture (HPLM)	Same as HPLU except 25–60% of O_3 estimated from stratosphere based on PV.
High Ozone Plume-SINF (HPLV)	Same as HPLU except more than 60% of O_3 estimated from stratosphere based on PV.
High Ozone (HO3)	$O_3 > 20\%$ above RP, $ASR_{VS} < 0.1$, and less than 25% of O_3 estimated from stratosphere based on PV.
High Ozone Mixture (HO3M)	Same as HO3 except 25–60% of O_3 estimated from stratosphere based on PV.
Stratospherically Influenced (SINF)	Same as HO3 except more than 60% of O_3 estimated from stratosphere based on PV.

convective outflow/clean Pacific air (CON/CP) can be seen in the lower free troposphere at the beginning of the flight and very extensively in the upper troposphere (>9 km) across the entire flight.

[30] The result of applying these air mass categories to the data from TP and PWB in the western Pacific is shown in Figure 11. Two latitude regions were used to bin the observations of these air masses, and these observations were also binned by altitude in 1-km intervals. The bar charts present the percentage of the observations that were made in a latitude and altitude bin for each air mass type. Also, provided along the side of each chart is the percentage for each air mass type observed over the entire 0–18-km altitude range. For TP in the low-latitude range (14–25°N), the enhanced O_3 with enhanced aerosol categories of HPLU and HPLM dominated the air mass types in the free troposphere below 5 km. In the middle-to-upper troposphere (5–12 km), the enhanced O_3 air masses were mostly dominated by HO3, which is associated with photochemical production of O_3. The low-O_3 air category CON/CP dominated the observations in the upper troposphere (>9 km) and the overall observations across the entire troposphere at 34%. The high O_3 cases represent 31% of the observations with about half of these also with enhanced aerosol loading (15%). An estimate of the observations that are attributed to the troposphere and stratosphere can be made by weighting the observations in each high O_3 category by the average fractional O_3 amount from those two sources based on the criteria given in Table 1 (assumes average of range of stratospheric O_3 contribution in each case). Using this method, and adding the individual contributions together gives the estimate that 18% of the observations are from the troposphere and 13% are from the stratosphere.

[31] In the midlatitude range (25–46°N) during TP, the enhanced O_3 with enhanced aerosol air masses (HPLU, HPLM, and HPLV) dominated the free troposphere observations up to about 10 km, and in this altitude range, HPLM dominated in the lower part and HPLV dominated in the upper part, as would be expected since HPLV has more stratospherically derived air than the HPLM category. In the 11–15-km region, the low-O_3 convective outflow (CON/CP) was frequently observed, while above 15 km, stratospherically influenced air (SINF) dominated the observations. For the entire altitude region, the high O_3 categories dominated all the observations at 63% with most of the observations associated with enhanced aerosols (36%). In addition, most of the high aerosol cases (31%) were either HPLM or HPLV cases with varying amounts of stratospheric air in them. Using the method described above, the estimated amount of tropospheric and stratospheric observations in the high O_3 air was found to be 28 and 35%, respectively. This is a significant increase from what was found in the lower latitudes during TP.

[32] The air mass characterization was done with the same criteria for PWB, and the results are also presented along with TP in Figure 11. During PWB at low latitudes, the enhanced O_3 categories were confined below 9 km with comparable amounts of observations for enhanced O_3 air with (HPLU) and without (HO3) aerosols. In this same region, there were few observations of stratospherically enhanced air masses (HPLM, HPLV, HO3M, and SINF were <4.1%). Convective outflow of low-O_3 air (CON/CP) dominated all the categories in the upper troposphere (9–15 km), and the SINF category started to come in just under the tropopause. The column average of the observations for the enhanced O_3 categories for this region was 23% with 15% attributed to the troposphere and 8% to the stratosphere. Compared to PWB, TP had a relative increase in the observation of enhanced O_3 air masses by 30%, and the relative increase in the tropospheric and stratospheric components of these observations were 20% and 62%, respectively.

[33] In the midlatitudes for PWB, nearly all of the observations of enhanced O_3 were in categories that were associated with enhanced aerosols and some component of stratospheric air (HPLM and HPLV), and they were mostly found in the free troposphere below 10 km. In this same altitude range, there was a significant fraction of the air masses that did not contain enhanced O_3 relative to the reference profile but did have enhanced aerosols in it (BPLU). This would be more associated with continental dust or pollution, but without significantly enhanced O_3. In the upper troposphere, the low-O_3 convective outflow dominated the observations up to about 14 km when the SINF category became the most prevalent. Over the entire troposphere in this region, the amount of observations of enhanced O_3 air masses was 41% with 15% attributed to the troposphere and 26% attributed to the stratosphere. Compared to PWB, TP had a relative increase of 54% in observed enhanced O_3 air masses, and for these air masses, the relative increase for the tropospheric component was 87% and for the stratospheric component was 35%. It was previously discussed that the average PV distributions between TP and PWB showed that there was more STE occurring during TP than in PWB, and this is further confirmed by comparing the air mass characterization results between the two field

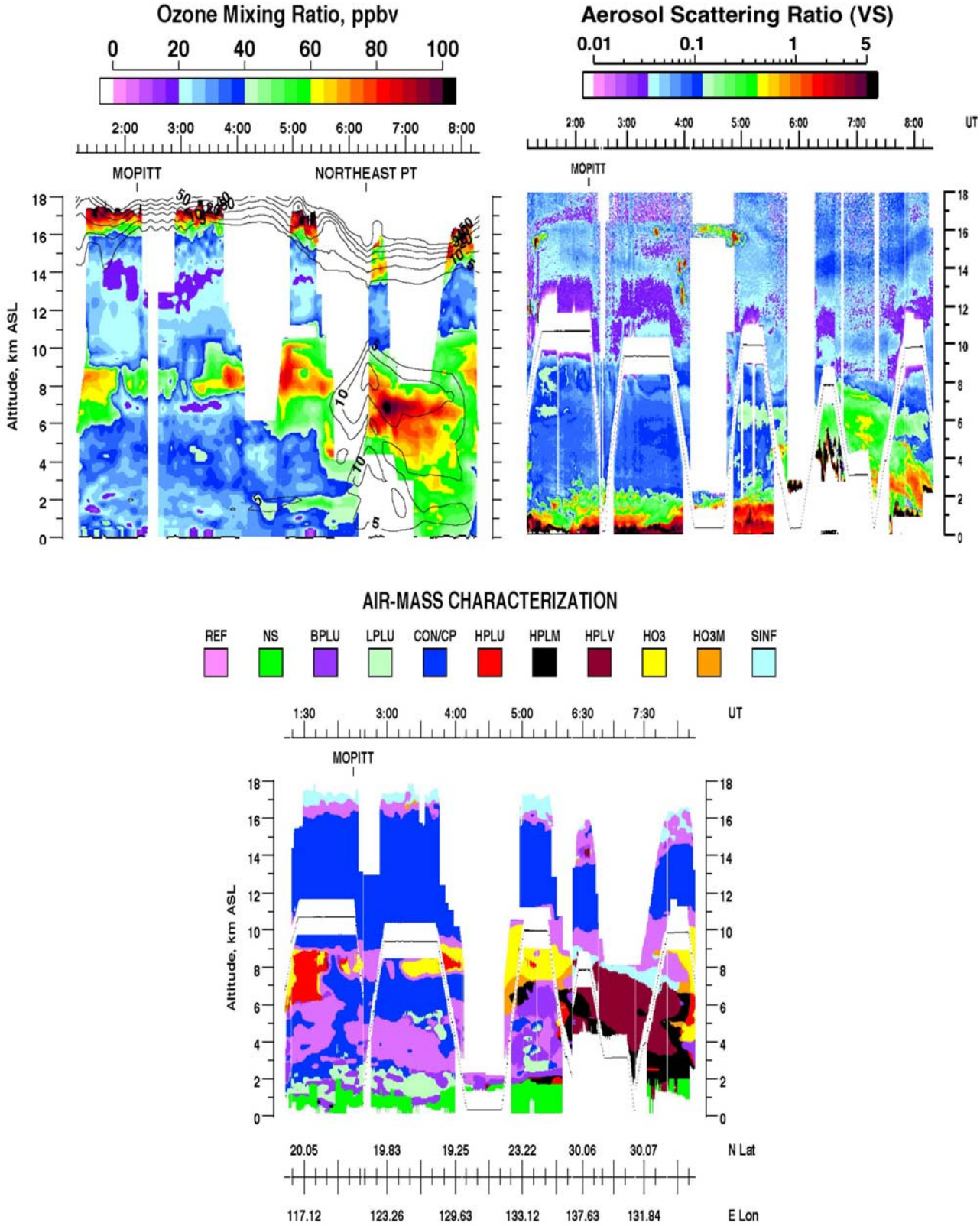

Figure 10. Ozone with PV isopleths in PVU (top left), aerosol scattering ratios (top right), and air mass characterization (bottom) for flight from Hong Kong to Okinawa on 17 March 2001 (Flight 11).

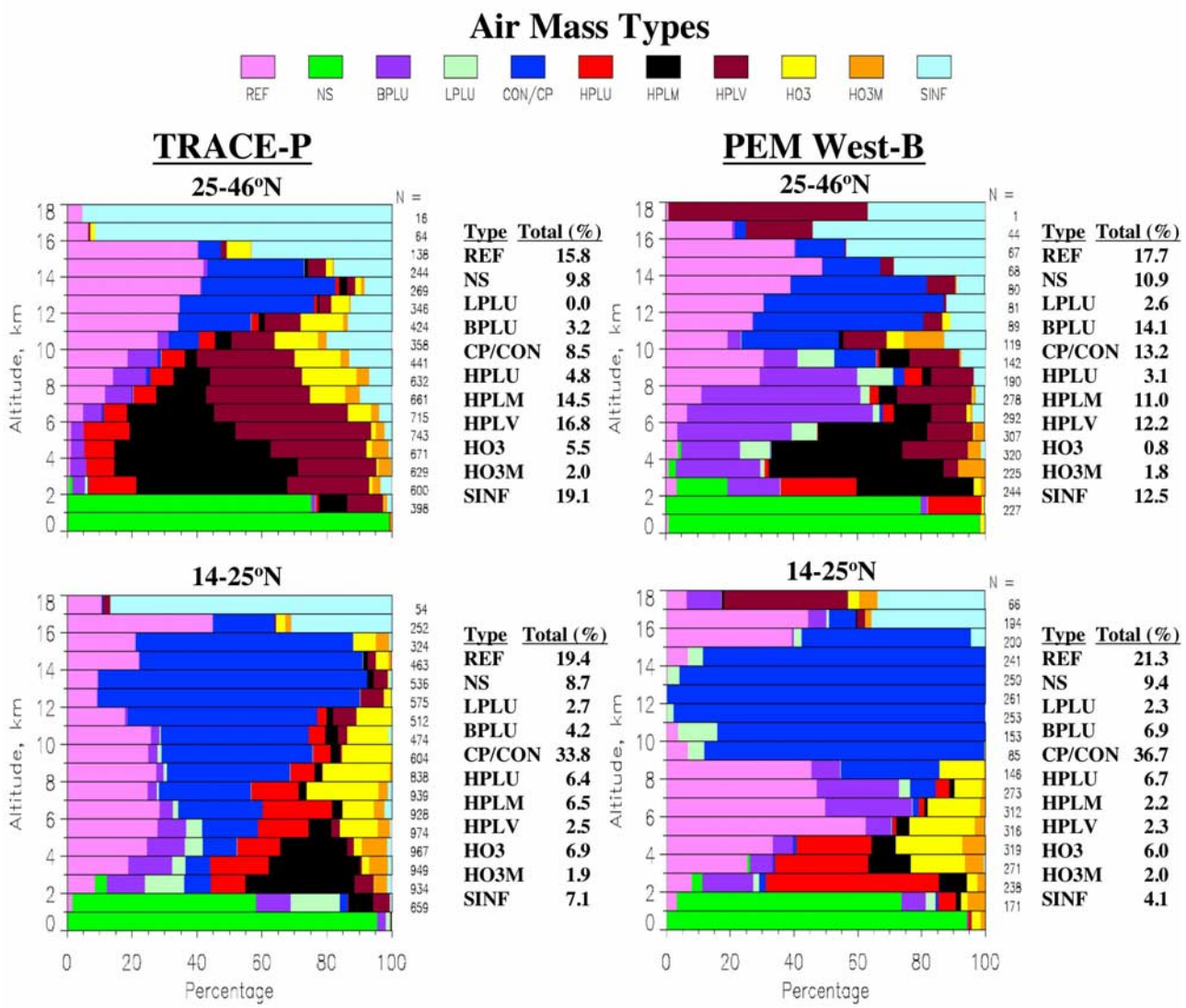

Figure 11. Percentage of time air mass types were observed during TRACE-P and PEM West-B in the low (14–25°N) and middle (25–46°N) latitude regions over the western Pacific (west of 150°E).

experiments. While the STE increased between TP and PWB, it is also clear from the above analysis that the amount of enhanced O_3 air that is attributed to tropospheric origin also increased significantly between PWB and TP. This increase may be attributed to the increased photochemical activity that was present during TP compared to PWB [*Miyazaki et al.*, 2002; D. D. Davis et al., An assessment of trends in western North-Pacific ozone photochemistry based on by observations from NASA's PEM-West B (1994) and TRACE-P (2001) field studies, submitted to *Journal of Geophysical Research*, 2003, hereinafter referred to as Davis et al., submitted manuscript, 2003].

3.3.2. Aerosol Air Mass Characterization

[34] The aerosol characteristics of all the air mass categories were determined for the airborne lidar measurements of aerosol backscattering at multiple lidar wavelengths (ASR_{IR} and ASR_{VS}), their derived WVD, and DPL from the nadir VS lidar measurements. The aerosol characteristics were derived from all flights west of 150°E. The WVD was calculated from coincident ASR_{IR} and ASR_{VS} measurements when $ASR_{IR} > 0.2$ and $ASR_{VS} > 0.1$, but when the coincident sample size was small (<100), the WVD was calculated directly from the median values of ASR_{IR} and ASR_{VS}. Aerosol DPL values were also only calculated for cases where $ASR_{VS} > 0.1$. The aerosol characteristics for TP and PWB are given in Table 2. TP results are presented for all the aerosols that were observed in each category and for only those aerosols that had high DPL (>5%). The results from PWB include ASR_{IR}, ASR_{VS}, and WVD, but no DPL measurements were made during PWB.

[35] The lowest aerosol scattering values for TP were associated with the HO3, HO3M, SINF, REF, and CON/CP categories with $ASR_{IR} < 0.24$ and $ASR_{VS} < 0.07$ (all values given below are median values). CON/CP had the lowest values of ASR_{IR} and ASR_{VS} of 0.1 and 0.04, respectively, which is consistent with the air in the upper troposphere having the lowest aerosol loading in association with cirrus cloud cleansing. The large WVD (1.9–2.5) associated with aerosols in these low aerosol scattering air masses indicates that they are predominantly submicron in size. Air mass

Table 2a. Aerosol Characteristics By Air Mass Category (AMC) Given for All Aerosols Observed in TP[a]

	ASR-IR				ASR-VS				WVD					DPL			
AMC	Median	Mean	σ	N	Median	Mean	σ	N	Median	Mean	Cal.	σ	N	Median	Mean	σ	N
REF	0.18	0.17	0.5	6471	0.05	0.06	0.1	7604	–	–	2.39	–	85	–	–	–	–
NS	17.8	19.3	12	2295	1.66	1.83	1.1	2360	0.28	0.35	0.01	0.4	2082	7.6	10.6	10	222
BPLU	0.68	1.98	4	1884	0.19	0.32	0.4	2277	1.72	1.64	1.85	0.8	1513	2.3	3.5	5	139
LPLU	0.61	1.36	4	920	0.16	0.24	0.4	989	1.41	1.52	1.75	0.7	713	2	2.4	3	829
CON/CP	0.1	0.13	0.5	8526	0.04	0.05	0.05	9590	–	–	2.46	–	52	–	–	–	–
HPLU	1.17	3.43	6	2778	0.26	0.45	0.5	3560	1.66	1.6	1.47	0.8	2525	2.5	5.6	7	188
HPLM	1.89	4.23	6	5453	0.35	0.57	0.6	6079	1.17	1.25	1.16	0.8	4981	4.5	7.2	7	425
HPLV	1.43	3.28	6	3607	0.3	0.5	0.6	4638	1.56	1.55	1.37	0.8	3258	6.2	8.8	8	222
HO3	0.19	0.2	0.1	2775	0.07	0.07	0.02	3256	–	–	2.30	–	66	–	–	–	–
HO3M	0.24	0.49	1.1	920	0.07	0.07	0.1	1094	–	–	1.93	–	62	–	–	–	–
SINF	0.17	0.38	0.7	1037	0.05	0.06	0.04	1764	–	–	1.94	–	25	–	–	–	–

Table 2b. Aerosol Characteristics By Air Mass Category (AMC) Given for Only High Depolarizing Aerosols (>5%) Observed in TP[a]

	ASR-IR				ASR-VS				WVD					DPL			
AMC	Median	Mean	σ	N	Median	Mean	σ	N	Median	Mean	Cal.	σ	N	Median	Mean	σ	N
NS	20.6	22.5	12	1388	1.88	2.01	1.1	1456	0.09	0.24	−0.03	0.3	1319	12.5	14.8	9	146
BPLU	1.93	5.94	9	235	0.3	0.62	0.8	243	0.79	0.86	0.87	0.6	211	6.6	10.1	8	246
HPLU	4.68	7.97	8	514	0.65	0.91	0.8	529	0.68	0.77	0.68	0.6	504	13.7	15.1	8	530
HPLM	2.93	6.06	8	1847	0.47	0.73	0.8	1875	0.85	0.83	0.92	0.6	1745	10.4	12.4	7	188
HPLV	2.92	5.79	8	1261	0.52	0.79	0.8	1280	1.16	1.14	1.1	0.7	1172	10.2	13.4	9	128

Table 2c. Aerosol Characteristics By Air Mass Category (AMC) Given for All Aerosols Observed in PWB[a]

	ASR-IR				ASR-VS				WVD				
AMC	Median	Mean	σ	N	Median	Mean	σ	N	Median	Mean	Cal.	σ	N
REF	0.16	0.19	0.2	3015	0.07	0.08	0.07	3063	–	–	2.61	–	67
NS	8.6	10.1	7	1319	1.03	1.19	0.8	1195	0.39	0.5	0.43	0.5	1054
BPLU	0.96	1.44	3	2281	0.21	0.28	0.3	2309	1.46	1.51	1.44	0.5	1754
LPLU	0.82	0.98	0.9	477	0.13	0.2	0.2	489	1.64	1.87	0.9	0.7	402
CON/CP	0.14	0.15	0.08	3636	0.07	0.07	0.02	3800	–	–	2.83	–	31
HPLU	5.15	8.17	9	892	0.77	1.1	1	873	0.81	0.96	0.8	0.7	763
HPLM	0.93	2.79	4	1441	0.22	0.47	0.6	1455	1.48	1.5	1.57	0.6	1320
HPLV	0.64	1.06	1.3	984	0.18	0.24	0.2	978	1.86	1.81	1.87	0.6	877
HO3	0.17	0.27	0.5	663	0.07	0.08	0.1	693	–	–	2.51	–	17
HO3M	0.29	0.86	2	377	0.08	0.09	0.06	370	–	–	1.83	–	47
SINF	0.19	0.23	0.2	714	0.07	0.07	0.03	716	–	–	2.32	–	41

[a]The median, mean, standard deviation (σ), and number (N) of independent measurements are given in each category. Calculated (Cal.) WVD from ASR median values is also given.

categories that have enhanced aerosol loading were found to have different aerosol characteristics depending on the amount of O_3 in the air mass. In the enhanced O_3 categories (HPLU, HPLM, and HPLV), the aerosols had significantly higher scattering ratios and DPL values than the air masses with background (BPLU) and low-O_3 (LPLU) levels. The WVD is similar between the different enhanced aerosol categories so there is some commonality in the aerosol size distributions in these air masses even though there may be differences in the number densities of the aerosols. NS had the largest aerosol scattering ratios, lowest WVD, and highest DPL of all the categories. This is to be expected because of the relative humidity growth of aerosols in the lower troposphere and in particular in the MBL. This growth produces large particles which are efficient scatterers with low WVD, but there are also depolarizing dust and sea salt aerosols in the lowest 2 km which contribute to the enhanced DPL in this category.

[36] Limiting the examination of TP aerosols to those in each category that had enhanced DPL (>5%) results in the aerosol characteristics shown in Table 2b. The NS and plume categories (BPLU, HPLU, HPLM, and HPLV) were the only ones that had enhanced DPL aerosols. Compared to all the aerosols in the same air mass type, the aerosols with enhanced DPL had significantly larger aerosol scattering ratios (>2X for ASR_{IR} and >1.5X for ASR_{VS}), significantly lower WVD (generally less than 1), and significantly higher DPL (greater than ∼10%). This indicates that the depolarizing aerosols are much larger then the average aerosol composition in the air mass types, which further reflects that the aerosol composition is made up of a wide range of aerosol characteristics.

[37] The aerosol characteristics for PWB are presented in Table 2c for comparison with TP results. The general scattering characteristics for the low aerosol loading air mass types (HO3, HO3M, SINF, CON/CP, REF) are comparable to the TP results. Aerosols in the HPLU air mass type had scattering ratios more than a factor of 4 larger than observed in TP and the WVD is a factor of 2 lower. This indicates much larger aerosols were found in this category during PWB. The

opposite was found in the HPLM and HPLV categories with lower scattering ratios and higher WVD. This is consistent with there being less STE and less coupling with continental pollution, including desert dust, during PWB.

3.3.3. Chemical Air Mass Characterization

[38] A detailed chemical composition was determined for each air mass type by averaging in situ chemical measurements across air masses that had been remotely categorized using the methodology described above. In this process, the observed air mass type had to be sufficiently large so that there was high confidence that the in situ measurements were being made in the specific air mass type. The in situ measurements were averaged over each air mass sample for each air mass type. The range of in situ measurements made on the DC-8 during TP and PWB are described by *Jacob et al.* [2003] and *Hoell et al.* [1997], respectively. This approach for defining the chemical characteristics of air mass types has been used extensively in other tropospheric chemistry investigations [*Browell et al.*, 1996a, 1996b, 2001; *Fenn et al.*, 1999].

[39] Table 3 presents the results from this analysis for TP air mass types. It should be noted that there were no cases where we confidently sampled in situ the enhanced O_3 mixture (HO3M) category so it is omitted from the table, and the low-O_3 plume (LPLU) category only had one case for its characterization. All of the other air mass types were represented by at least three independent in situ measurement periods or ''samples.'' In general, the median value for the sample set for each air mass type is given in the table to avoid the biasing of the averages by possible extreme values that might infrequently be encountered; however, when there were less than five samples, the average value is given. The latitude range of the samples is provided for each air mass type, and it can be seen that the samples for the low and background O_3 categories (REF, CON/CP, LPLU, BPLU) were obtained in the low-latitude range (<25°N) while all the other categories were mostly in the midlatitude range (>25°N). The exception to this was the HO3 category, which spanned the 20–29°N range. The altitude range of the samples also generally reflected where the air mass types were located (within the 12-km range of the DC-8), as seen in Figure 11. Of all the air mass types, the NS air exhibited the highest levels of pollution related gases and aerosols, as would be expected in the low-altitude outflow from Asia, and the hydrocarbon ratios indicated that this was the air mass containing the most recent pollution emissions. By contrast, the CON/CP air had very low levels of O_3 and CO and the lowest levels of hydrocarbons of any of the air mass types, and the hydrocarbon ratios indicate that this air had been over the marine environment for the longest time, which is consistent with it being considered as convective outflow of clean Pacific air. The air mass types that require special attention are associated with the enhanced O_3 categories. All of the HPL categories have similar O_3, CO, hydrocarbon, PAN, and SO_2 levels, which are significantly elevated from the background O_3 categories (REF and BPLU). In addition, C_2Cl_4 is significantly enhanced in these air masses which also indicates a strong urban pollution influence. The aerosol related compounds of nitrate and sulfate are all high in the HPL categories. The hydrocarbon ratios reflect some air mass processing, and the higher O_3/CO ratio indicates recent photochemical O_3 production. There are clearly differences in the sources contributing to the HPL categories, and it is not a simple chemical transition from HPLU to HPLM and HPLV with a mixing-in of stratospheric air defined as SINF. The atmospheric conditions that lead to these different subcategories probably favor different source regions. There are indications from the values of ^{7}Be, HNO_3, and NO_2 that HPLV has more stratospheric air mixed in with it than for HPLM or HPLU, but HPLV also has high levels of C_2Cl_4, nitrate, and sulfate, which indicates a high level of tropospheric pollution in these air masses. This is clearly a case of a difference in the source region for the different HPL categories. The enhanced O_3 with low aerosol loading categories of HO3 and SINF are quite different from the HPL air mass types. The HO3 category has significantly less CO, hydrocarbons, PAN, C_2Cl_4, CH_3I, $CHBr_3$, nitrate, and sulfate, and the hydrocarbon ratio indicates an air mass which has undergone much more processing. There were significant increases in OH and NO, and the O_3/CO ratio was the highest of the nonstratospheric air mass types. This indicates active photochemistry and long-range transport of these air masses. The elevated amount of acetonitrile and low level of H_2O_2 could be associated with the convective transport of biomass burning gases into the midtroposphere as was discussed for the data shown in Figure 2. The SINF category had a composition that was more polluted than found in previous results [*Browell et al.*, 1996a, 2001; *Fenn et al.*, 1999]. While O_3, ^{7}Be, and HNO_3 were generally higher, H_2O, CO, CO_2, CH_4, nonmethane hydrocarbons, H_2O_2, sulfate, and nitrate were generally lower but not as low as expected at this level in the lower stratosphere. The presence of enhanced pollution related gases and aerosols in the SINF category reflects the mixing of tropospheric pollution into the lower stratosphere [*Pierce et al.*, 2003; Avery et al., submitted manuscript, 2003]. This can account for some of the remaining pollutants in the HPLV category, which is composed of a large fraction of air from the lower stratosphere. The background and low-O_3 categories (REF, BPLU, and LPLU) all had intermediate composition from the extremes discussed above, and while the aerosol loading was different between them, they otherwise had similar chemical compositions.

[40] The composition of the air mass types observed during PWB is presented in Table 4. A comparison of the compositions for PWB and TP show some very significant differences. Except for the NS and SINF categories, PWB had higher levels of nearly all the pollution related gases and aerosols compared to TP, including CO, all hydrocarbons, PAN, SO_2, HNO_3, H_2O_2, C_2Cl_4, nitrate, and sulfate, and higher levels of the hydrocarbon ratios. The only values that were lower in all air mass types in PWB compared to TP were CO_2 and CH_4, which is not surprising since their concentrations are increasing worldwide. It was also found that O_3 and the O_3/CO ratios were lower in all the enhanced O_3 air mass types in PWB, with the exception of SINF, which was measured farther into the lower stratosphere in PWB. The above differences generally reflect less photochemical activity during PWB compared to TP, which is supported by the photochemical analysis of the two campaigns by Davis et al. (submitted manuscript, 2003), but some of the differences can also be associated with increased STE in TP, which was discussed above and

Table 3. TRACE-P Air Mass Composition[a]

	REF (3)	NS (31)	CON/CP (18)	LPLU (1)	BPLU (3)	HPLU (9)	HPLM (22)	HPLV (16)	HO3 (11)	SINF (5)
Lat. Range, °N	21–23	14–40	14–24	20	20–25	23–44	20–39	22–43	20–29	25–36
Radar Alt., km	6.72	0.34	9.57	4.42	3.32	7.01	3.89	5.50	8.51	7.89
H_2O, ppmv	2325	10700	280	6100	7800	350	750	910	280	24
O_3, ppbv	41.4	53.0	27.6	24.6	37.0	65.2	57.4	62.7	65.6	209
CO, ppbv	99.3	200	79.9	83.9	121	123	125	128	91.3	77.4
CH_4, ppbv	1755.0	1836.1 (30)	1751.2 (14)	1754.6	1770.7	1768.2	1786.0 (20)	1789.4	1752.0 (10)	1740.6
CO_2, ppmv	371.3	376.3	371.3 (17)	–	372.6	372.7	373.1	373.2	370.8	370.4
C_2H_2 (ethyne)	129	600	59.0 (17)	87.0	170	260	284 (21)	262	107	80.5
C_2H_6 (ethane)	576	2060	462 (17)	508	677	911	1292 (21)	1201	532	544
C_3H_8 (propane)	48.2	658	23.1 (17)	31.7	54.5	117	257 (21)	238	35.3	66.5
PAN	84.3	540	16.0 (17)	5.0	31.3	222	148 (21)	173	139 (9)	130
SO_2	6.9	283	6.5 (15)	5.0	142.5	8.2	25.4 (19)	20.0	13.5 (7)	11.1
Acetonitrile	147	110 (25)	114 (13)	115	156.1	187 (8)	130 (21)	128 (14)	189 (8)	148
NO	34.7	21.8 (28)	26.2 (14)	3.6	4.4 (2)	20.9 (8)	15.3 (18)	23.0 (14)	56.1 (9)	44.9
NO_2	14.3 (2)	92.8 (24)	6.8 (10)	5.5	2.3 (1)	14.7 (7)	20.5 (15)	29.6 (14)	29.6 (8)	40.7 (4)
HNO_3	183	458	67.2 (16)	138	641	140	146 (19)	158	193 (8)	585
OH	0.18	0.12	0.14	0.04	0.16	0.08	0.05	0.06	0.13	0.10
HO_2	16.5	11.4	9.0	6.2	18.3	8.1	6.9	6.4	7.0	4.4
H_2O_2	1183 (2)	714	306 (13)	953	2694 (2)	404 (7)	472 (19)	374 (14)	203 (8)	83.5 (4)
HCHO	76 (2)	440 (23)	72 (15)	109	240	<50 (8)	167 (12)	83 (11)	<50 (8)	93
CH_3Cl	566	556	539 (17)	550	568	574	548 (21)	558	571	518
CH_3Br	8.1	9.0	7.8 (17)	8.3	8.0	8.6	8.7 (21)	8.6	8.1	8.3
CH_3CCl_3	39.2	41.2	39.0 (17)	39.3	38.9	39.1	39.8 (21)	40.0	38.5	38.5
CH_3I	0.13	0.45	0.06 (17)	0.10	0.19	0.10	0.11 (21)	0.13	0.04	0.02
$CHBr_3$	0.41	1.38	0.51 (17)	0.54	0.43	0.62	0.69 (21)	0.77	0.32	0.22
C_2Cl_4	2.8	11.4	2.3 (17)	2.6	3.0	3.1	5.0 (21)	5.6	1.7	2.0
UFA, cm^{-3}	1580	1350	3740	833	575	1640	811 (20)	982	1640	691
FAU, cm^{-3}	457	652 (26)	747	88	269	966	731 (16)	542 (12)	956	249
Nitrate	–	455	1.0 (7)	–	32.0 (1)	45.0 (1)	44.0 (10)	156 (5)	4.2 (3)	10.4 (3)
Potassium	–	192 (30)	1.0 (7)	–	48.0 (2)	23.0 (2)	32.0 (11)	38.0 (7)	11.1 (3)	1.0 (4)
Sulfate	–	1140	30 (7)	–	254 (1)	108 (1)	307 (10)	396 (6)	55 (3)	111 (3)
^7Be, fCi/scm	–	202 (26)	187 (7)	–	317 (1)	301 (1)	210 (9)	528 (5)	694 (3)	5200 (3)
HCFC-22	146.1	158.0	144.2 (17)	148.0	146.5	147.5	152.0 (21)	150.4	142.0	142.0
FAU/UFA	0.46	0.62 (26)	0.19	0.12	0.43	0.69	0.78 (16)	0.62 (12)	0.65	0.42
C_2H_2/CO[b]	1.19	3.30	0.78 (17)	0.98	1.28	1.92	2.20 (21)	2.12	1.16	1.26
C_3H_8/C_2H_6	0.071	0.320	0.050 (17)	0.059	0.070	0.131	0.198 (21)	0.188	0.068	0.130
O_3/CO	0.43	0.24	0.30	0.30	0.34	0.54	0.46	0.50	0.71	2.7
SO_4/O_3[b]	–	26	1.3 (7)	–	6.4 (1)	1.8 (1)	5.6 (10)	6.0 (6)	0.9 (3)	0.5 (3)
NO_2/O_3[b]	0.36 (2)	1.94 (24)	0.25 (10)	0.24	0.06 (1)	0.21 (7)	0.36 (15)	0.47 (14)	0.44 (8)	0.16 (4)
$^7Be/O_3$[c]	–	3.9 (27)	7.0 (7)	–	8.0 (1)	5.0 (1)	4.0 (9)	8.7 (5)	10.6 (3)	20.9 (3)

[a]Values are given in pptv unless otherwise noted, and number of independent cases sampled with in situ instruments on DC-8 is given in parentheses at top unless otherwise noted next to value. Median values are given when there were five or more independent cases sampled, and average values are given when fewer cases were sampled. Note that there were no in situ data available for HO3M air mass type.

[b]Units of pptv/ppbv.

[c]Units of (fCi/scm)/ppbv; FAU, ultrafine aerosols; UFA, unheated fine aerosols.

is addressed by *Pierce et al.* [2003]. Also, during PWB the NS air was slightly less polluted than for TP with lower CO, PAN, SO_2, HNO_3, nitrate, and sulfate. Except for the trends mentioned above, all the other air mass types had characteristics similar to those observed in TP.

3.4. Flux Estimates

[41] There is considerable interest in the transport of pollutants from Asia to the Pacific Ocean and North America, and a number of papers have discussed the transport of pollutants to Japan and the western Pacific Ocean [*Gregory et al.*, 1997; *Talbot et al.*, 1997; *Xiao et al.*, 1997; *Pochanart et al.*, 1999; *Phadnis and Carmichael*, 2000; *Bey et al.*, 2001]. As emissions increase in Asia, it is expected that pollution levels in North America will also increase due to long-range transport [*Jacob et al.*, 1999; *Jaffe*, 1999; *Yienger et al.*, 2000; *Kotchenruther et al.*, 2001; *Wilkening*, 2001]. One of the main objectives of TP was to determine the fluxes of O_3 and other gases that were advecting off of the Asian continent over the western Pacific. The following sections discuss the methodology and results for estimating the eastward flux of O_3, CO, CO_2, and CH_4 during TP.

3.4.1. Ozone Flux Estimates

[42] The eastward component of the O_3 flux for each TP flight was estimated by combining the tropospheric O_3 cross section determined from the combined lidar and in situ data along the flight track with the corresponding cross section of the westerly wind component from the ECMWF analysis. In this analysis, the flux is defined as the mass of a gas per unit time transported eastward through a defined area. The eastward O_3 flux distribution is calculated for each O_3 data interval (30 m in vertical and 2 s in horizontal) in the atmospheric cross section along the flight track. The flux per unit data interval is sensitive to the direction of the flight track as the projected north-south area of the data interval has to be used in the eastward flux calculation. Figure 12 presents an example of the cross sections used in the flux calculation and the resulting O_3 flux distribution for the flight from Guam to Hong Kong on 3–4 March 2001. The

Table 4. PEM West-B Air Mass Composition[a]

	REF (5)	NS (5)	CON/CP (4)	BPLU (13)	HPLU (7)	HPLM (2)	HPLV (3)	HO3 (4)	SINF (2)
Lat. Range, °N	16–28	15–29	9–25	27–45	16–28	22–31	43–46	13–20	38–45
Radar Alt., km	3.41	0.35	8.11	5.58	2.83	3.25	6.03	4.46	10.19
Dew pt. Deg C	−38.9	4.8	−36.1	−39.6	−1.8	−31.7	−56.5	−29.7	−64.2
O_3, ppbv	46.4	47.2	27.8	44.1	50.4	49.8	63.9	56.7	375
CO, ppbv	91.9	159	86.0	152	240	145	144	100	41.9
CH_4, ppbv	1735.8 (4)	1786.8	1717.0	1770.0	1763.2 (3)	1763.3	1768.2	1719.4	1631.9
CO_2, ppmv	358.7	361.5	358.0	360.8	361.5	360.5	360.7	358.6	355.5
C_2H_2 (ethyne)	97.4	572	77.7	477	794	458	444	122	12.6
C_2H_6 (ethane)	704	1890	558	1650	1640	1500	1700	704	139
C_3H_8 (propane)	91.9	666	52.2	445	314	403	564	82.5	14.7
PAN	151	294	29.8	266	595 (5)	285	254 (2)	88.1 (3)	38.0
SO_2	45.6 (4)	62.0	22.4	47.9 (11)	40.0 (6)	38.2	–	22.2 (3)	54.1
NO	20.6	18.3	62.6	11.2	32.4	18.2	12.2 (1)	21.2	43.1 (1)
NO_y	632	683	349	670	1590	761	687 (1)	421 (3)	1610 (1)
HNO_3	199.8 (3)	118	186 (3)	148 (7)	974 (6)	196 (1)	–	303 (2)	1766
H_2O_2	258	337	588	394 (12)	3080	565	113	813	98.7
CH_3Cl	558	554	565	585	636	570	557	562	478
CH_3Br	9.4	10.5	9.7	12.0	11.2	10.1	11.8	10.0	8.3
CH_3CCl_3	119	134	119	126	122	126	120	119.8	88 (1)
CH_3I	0.07	0.43	0.10	0.14	0.48	0.13	0.09	0.08	0.05
C_2Cl_4	6.2	18.8	4.6	13.0	8.9	11.4	12.0	5.5	1.83
Aerosol, cm^{-3}	556	844	639	442	1360	596	259 (1)	454	108 (1)
Nitrate	57 (2)	112 (4)	5.8 (2)	60.0 (5)	87 (2)	–	–	<5.0 (1)	<5.0 (1)
Potassium	115 (2)	33 (4)	<25 (2)	37.8 (5)	206 (2)	–	–	<25 (1)	<25 (1)
Sulfate	124 (2)	306 (4)	9.4 (2)	273 (5)	274 (2)	–	–	12.0 (1)	169 (1)
^{7}Be, fCi/scm	175 (2)	198 (4)	95 (2)	186 (5)	227 (2)	–	–	442 (1)	3760 (1)
C_2H_2/CO[b]	1.05	3.67	0.90	3.45	3.32	3.10	3.03	1.16	0.27
C_3H_8/C_2H_6	0.123	0.361	0.091	0.265	0.178	0.250	0.316	0.108	0.161
O_3/CO	0.43	0.30	0.32	0.29	0.27	0.35	0.51	0.58	9.8
SO_4/O_3[b]	2.6 (2)	6.7	0.3 (2)	6.1 (5)	5.7 (2)	–	–	0.4 (2)	0.7 (1)
NO_y/O_3[b]	12.5	15.7	12.1	15.1	32.7	15.2	13.2 (1)	7.2 (3)	5.9 (1)
$^7Be/O_3$[c]	3.7 (2)	5.4 (4)	3.7 (2)	4.4 (5)	4.7 (2)	–	–	7.3 (1)	15.1 (1)

[a]Values are given in pptv unless otherwise noted, and number of independent cases sampled with in situ instruments on DC-8 is given in parentheses at top unless otherwise noted next to value. Median values are given when there were five or more independent cases sampled, and average values are given when fewer cases were sampled. Note that there were no in situ data available for HO3M or LPLU air mass types.
[b]Units of pptv/ppbv.
[c]Units of (fCi/scm)/ppbv.

O_3 cross section along the flight track with isopleth overlays of the ECMWF westerly wind components is shown along with the calculated distribution of the derived eastward O_3 flux (kg/day) in each data interval. Note that the abrupt horizontal changes in the calculated O_3 flux are due to changes in flight direction, which changes the effective area of the data interval used to calculate the O_3 flux. The calculated O_3 flux is influenced greatly by the magnitude of the eastward wind component as can be seen in the figure with the resulting flux distribution being very similar to the strong westerly wind distribution associated with the subtropical jet. The change in wind direction to easterly on the east side of the low-level front at about 0300 UT (see discussion above for Figure 2) produces a negative eastward flux of low-O_3 air associated with clean marine air in the lower troposphere. There is also a change in wind direction at low latitudes below 2 km after 0600 UT, and this leads to a negative eastward flux in a much more polluted environment over the South China Sea.

[43] The average eastward O_3 flux in 1 km altitude × 1 deg latitude bins from each flight in the western Pacific (west of 150°E) were averaged together on an equally weighted basis to arrive at the average eastward O_3 flux distribution for TP shown in Figure 13. Also shown in Figure 13 is the average westerly wind distribution, which was obtained by binning and averaging the eastward winds for the same flights as used in the flux calculation. The average tropospheric O_3 flux distribution was highly correlated with the average wind distribution with the only major deviation being in the upper troposphere (>10 km) south of 32°N where the higher wind speeds are offset by the lower O_3 in that region. The maximum O_3 flux was near the core of the jet with values of about 40×10^6 kg/day/deg/km. The average easterly wind in the lower troposphere in the tropics produced the only persistent large-scale region with negative O_3 flux with a maximum of about -5×10^6 kg/day/deg/km. There was also a small region of negative flux in the upper troposphere near 45°N.

[44] The eastward O_3 flux distributions were also calculated for each air mass category observed during TP. The correlation between the O_3 flux and each air mass category was done for each flight, and these results were averaged to arrive at the average latitudinal distribution for the eastward O_3 flux for each air mass category. These results are shown in Figure 14 for nearly all of the air mass categories (NS and LPLU are not shown). This figure graphically shows where the various air mass types were observed and their relative contribution to the average O_3 flux distribution. The enhanced O_3 and enhanced aerosol categories (HPL) are shown at the top of the figure. The altitude of the maximum flux for the HPLU and HPLM categories was in the 4–6-km region over a broad latitudinal range north of 20°N. The influence of the higher wind speeds in conjunction with the stratospheric intrusions contributed to the higher fluxes (>25 × 10^6 kg/day/deg/km) at higher altitudes closer to the jet with the center of the HPLV flux near 8 km and

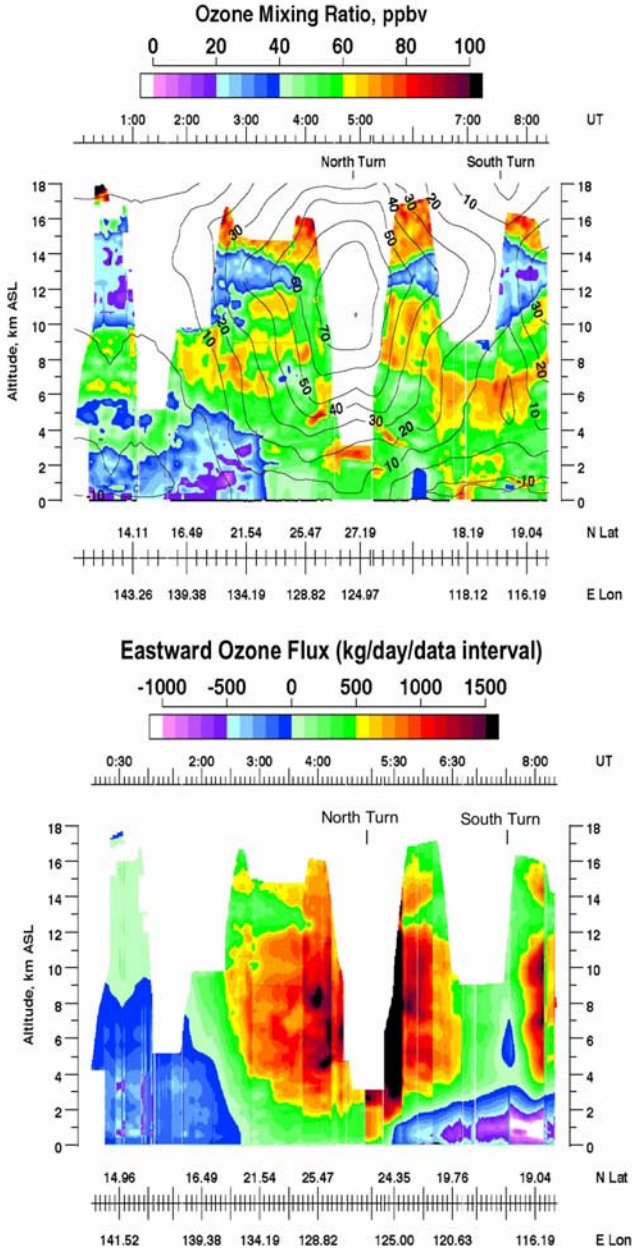

Figure 12. Example of eastward O_3 flux distribution (bottom) calculated from O_3 distribution observed on flight from Guam to Hong Kong on 3–4 March 2001 (Flight 6) (top) and westerly wind component (isopleth overlay, m/s). The eastward flux component is calculated at uniform data intervals along flight track, and thus the abrupt horizontal changes in the flux distribution are due to changes in flight direction (see Figure 2 for flight track and major turn points are indicated above).

35°N. The air masses with enhanced O_3 and low aerosol loading (HO3, HO3M, and SINF) showed a wide latitudinal variation in where they contribute to the O_3 flux. The HO3 flux was centered at about 8 km and 25°N with a maximum flux of about 8×10^6 kg/day/deg/km, and the SINF flux was mostly in the upper troposphere and near the core of the jet with a maximum flux on the order of 25×10^6 kg/day/deg/km near 11 km and 33°N. The CON/CP flux is concentrated in the upper troposphere (10–15 km) south of 31°N where the convective outflow of low-O_3 air was most prevalent. The BPLU category was generally lower in the troposphere (3–10 km) than the other air mass types and covered a broad latitudinal range from about 22–42°N. The REF flux was concentrated in the middle to upper troposphere (5–16 km) between 18 and 33°N with a maximum flux of about 10×10^6 kg/day/deg/km.

[45] The column tropospheric O_3 flux distributions for each air mass type and for all of them together are shown in Figure 15 along with the integrated tropospheric O_3 flux between 14 and 46°N. The latitude of the maximum O_3 flux for each air mass type directly reflects the dominant processes that contribute to creating it. For example, the HO3 category is centered at about 26°N with a peak flux of ~50 Gg/day/deg, and this has been predominantly associated with a biomass burning source in SE Asia [*Heald et al.*, 2003]. The HPLV category exhibited the greatest impact of all the air mass categories with the highest O_3 flux

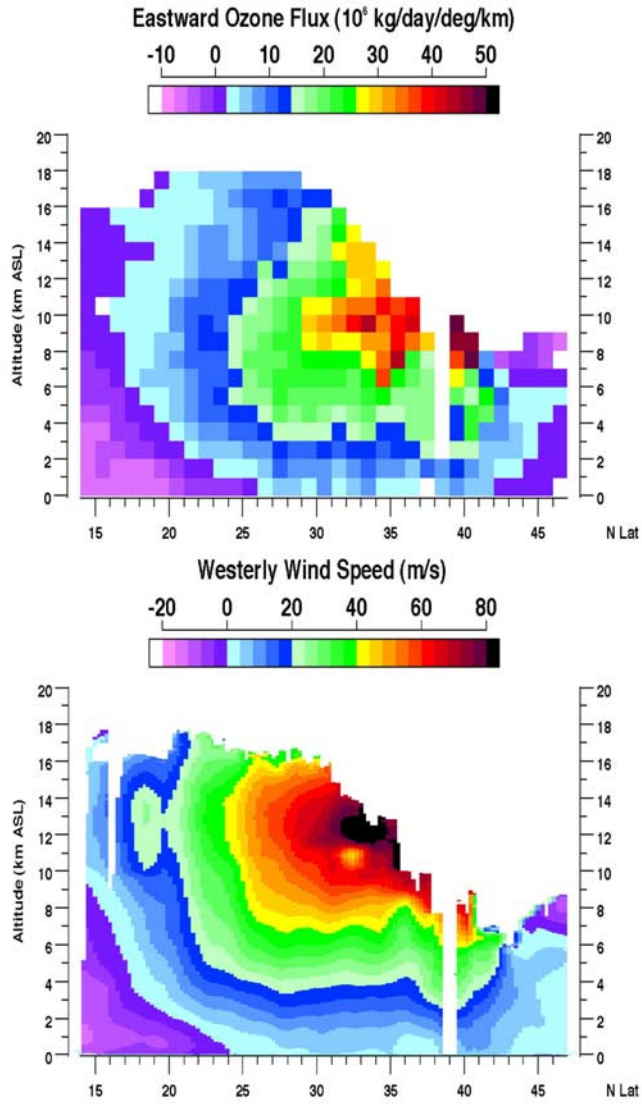

Figure 13. Average latitudinal eastward O_3 flux (top) and westerly wind speed distributions obtained on all TRACE-P flights west of 150°E.

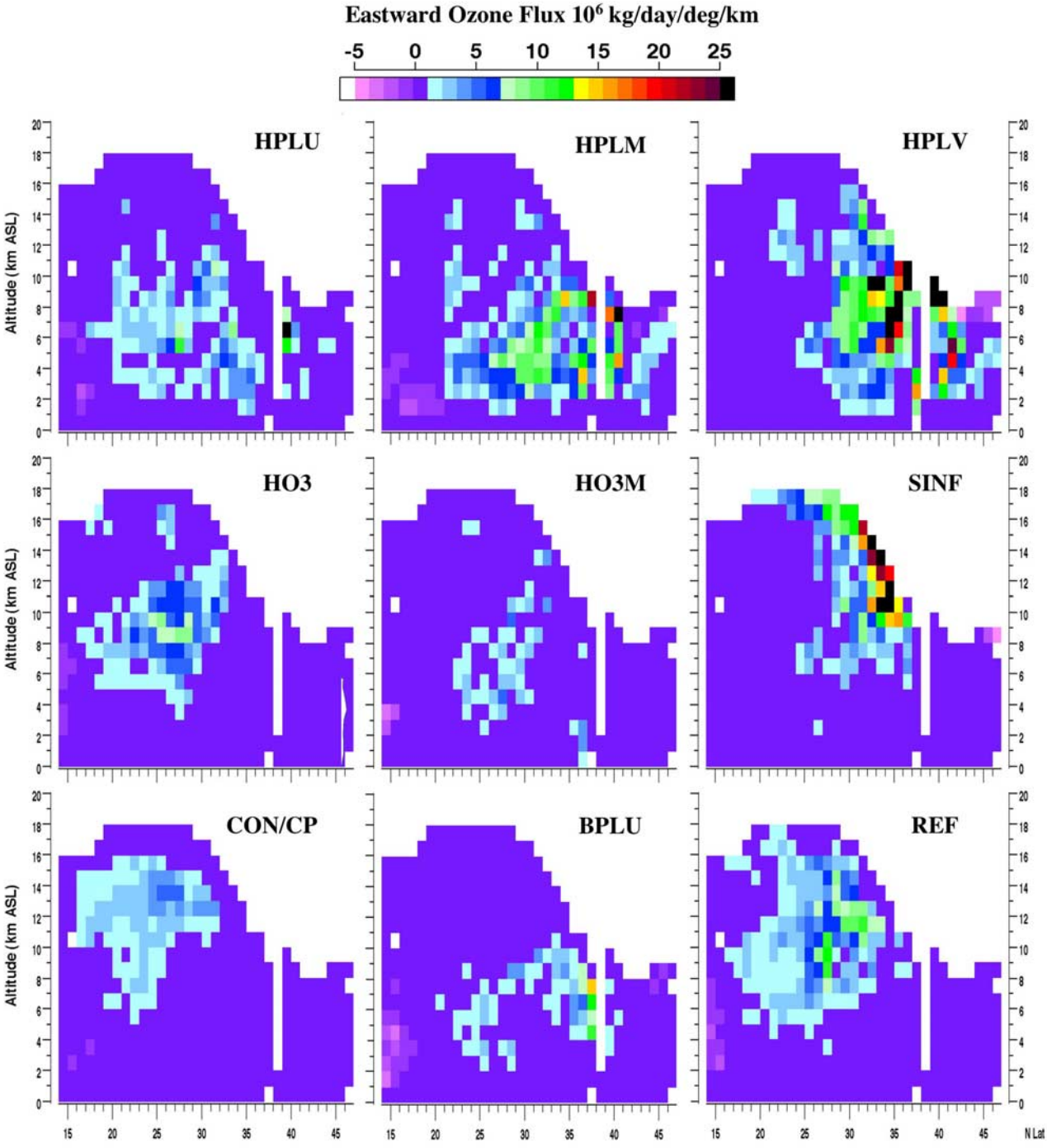

Figure 14. Eastward average O_3 flux by air mass category.

of 142 Gg/day/deg and the broadest flux distribution with an O_3 flux >50 Gg/day/deg over the entire region from 28 to 42°N. The HPLM category was similar in distribution to HPLV, but it had about half the flux levels. As was mentioned previously, the O_3 flux for SINF was narrowly focused on the 28–35°N region with a maximum O_3 flux of 117 Gg/day/deg. The total O_3 flux distribution was found to peak at 32°N at an O_3 flux of 342 Gg/day/deg. The general decrease in the total flux with increasing latitude from the peak was associated with the decreasing tropopause level and the decreasing wind speed north of the jet.

[46] The integrated O_3 flux is shown in the table in Figure 15. The total average O_3 flux between 14–46°N was found to be 5.15 Tg/day. HPLV had the highest O_3 flux with 1.51 Tg/day, and HPLM was second with 0.89 Tg/day. The two categories together represent 46% of the total O_3 flux. All of the high O_3 categories (HPLU, HPLM, HPLV, HO3, HO3M, and SINF) together represent 78% of the O_3

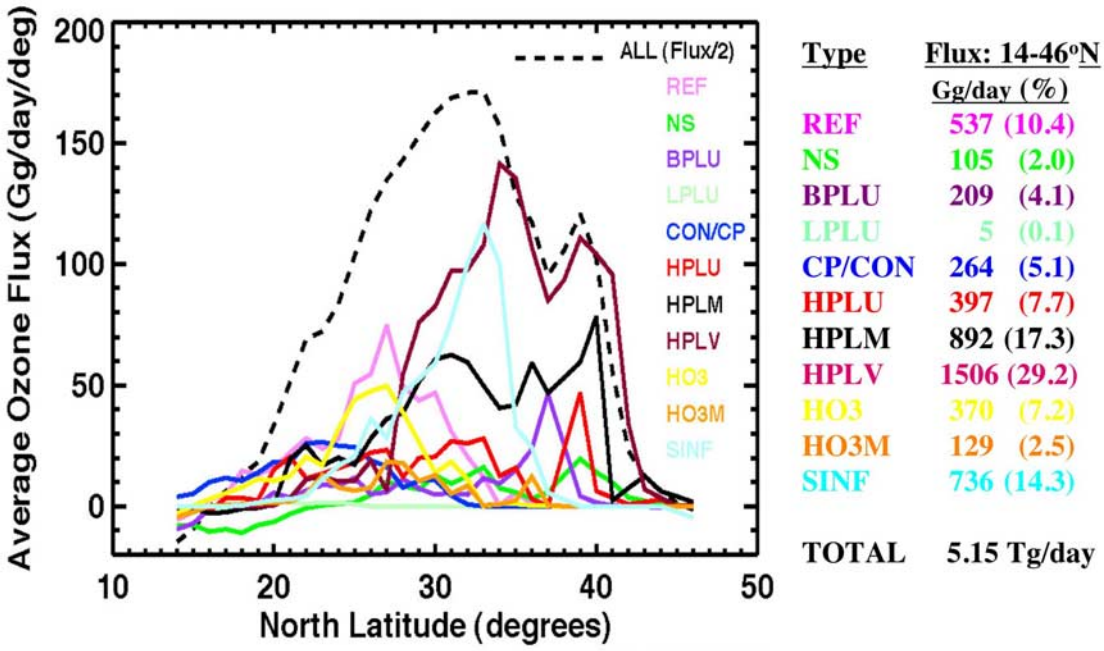

Figure 15. Average eastward tropospheric O_3 flux distribution by air mass type obtained west of 150°E and total O_3 flux by air mass type in 14–46°N region.

flux, and of those categories, it is estimated that about 58% of the flux was associated with stratospheric air.

3.4.2. O_3, CO, CO_2, and CH_4 Flux Estimates Based on Average Air Mass Compositions

[47] The total flux of O_3, CO, CO_2, and CH_4 were estimated for each air mass type by using the average air mass compositions identified in Table 3. These average gas concentrations for each air mass type were applied to all of the regions where that air mass type was observed on each flight (an example of the air mass type distribution was shown in Figure 10). The flux was calculated by applying the westerly wind component distribution to the different air mass types and their associated average gas concentrations for each flight and then combining these flux distributions in the same way that was done for deriving the average O_3 flux distribution discussed above. The flux in each air mass category was integrated in altitude across the troposphere and from 14 to 46°N to produce the resulting O_3, CO, CO_2, and CH_4 flux results for the individual air mass categories shown in Table 5a. These are total eastward flux estimates for these gases. The total flux of O_3 calculated with this method agrees to within ~11% of the total O_3 flux given in Figure 15 (without including HO3M). Even when the O_3 flux is compared in each of the air mass categories, the values are very similar with the only exception being in the SINF category where this second method estimates a significantly higher O_3 flux. In general, the O_3 flux comparison between the two methods provides confidence in using it for determining the flux of other gases.

[48] This technique was applied to determining the total flux for CO, CO_2, and CH_4, and their results are also shown in Table 5a. These total flux estimates are given by air mass type, and for these gases the largest fluxes were found in the HPLV and HPLM categories, which are generally associated with enhanced aerosol loadings and higher wind speeds (see Figure 14 for correlation to O_3 flux distributions). The estimated total flux of CO was 5.2 Tg/day (2.2 Tg-C/day), and again HPLV has the highest component of flux. The combination of HPLM and HPLV accounts for nearly half (48%) of the CO flux. Unlike O_3, where SINF had the third highest O_3 flux, the third highest CO flux was associated with the REF air mass type. The combination of all the air mass types with enhanced aerosols, including NS air, accounted for 67% of the CO flux. This indicates a strong influence from recent continental pollution emissions.

[49] The total flux estimates for CO_2 and CH_4 were found to be 27×10^3 Tg/day (7.4×10^3 Tg-C/day) and 47 Tg/day (35 Tg-C/day), respectively. The same major air mass types contributed in a similar way to the CO_2 and CH_4 fluxes as they did to the CO flux; however, due to the high background levels of CO_2 and CH_4, there were significant contributions to their total flux associated with nonpollution categories such as CON/CP and REF. It was found that the fluxes of all these gases were more influenced by the large variations in the eastward wind component between air mass types than the smaller variations in gas concentrations between them.

[50] The amount of O_3, CO, CO_2, and CH_4 flux contributed by Asia was estimated by calculating the background eastward flux of each gas and subtracting it from the total eastward flux of the gas. The background flux was determined by combining a uniform distribution of the background gas along the flight track with the wind analysis to come up with a background flux distribution for each flight. These distributions were averaged together in the same manner as for determining the O_3 flux to produce a background flux estimate for the gas which was then subtracted from the total flux to give an estimate of the Asian flux component. *Vay et al.* [2003] used the correlation between CO_2 and the C_2H_2/CO ratio in the near-Asia Tropical region to determine that the background level of CO_2 was approx-

Table 5a. Estimated O_3, CO, CO_2, and CH_4 Total Flux for TP Based on Average Air Mass Composition and Average Flux Estimated For Each Air Mass Type

AMC	O_3, Tg/day	CO, Tg/day	CO_2, 10^3 Tg/day	CH_4, Tg/day
REF	0.43	0.60	3.5	6.0
NS	0.11	0.23	0.7	1.2
BPLU	0.16	0.32	1.5	2.6
LPLU	0.00	0.01	0.0	0.1
CON/CP	0.24	0.41	3.0	5.2
HPLU	0.40	0.45	2.1	3.7
HPLM	0.82	1.04	4.9	8.5
HPLV	1.21	1.44	6.6	11.5
HO3	0.36	0.29	1.9	3.2
SINF	1.82	0.39	3.0	5.1
TOTAL[a]	5.55	5.18 (2.2 of C)	27.2 (7.4 of C)	47.1 (35 of C)

[a]Does not include HO3M category.

Table 5b. Asian Flux Estimate Based on Difference Between Total Eastward O_3, CO, CO_2, and CH_4 Flux (Table 4) and Estimated Eastward Background Flux For Each Gas

	Asian Flux (REF-Based Background[a]) (Tg/Day)	Asian Flux (CO_2-Based Background[b]) (Tg/Day)
O_3	2.26	–
CO	0.56 (0.24 of C)	0.34 (0.14 of C)
CO_2	–	18.0 (4.9 of C)
CH_4	–	0.076 (0.057 of C)

[a]Based on background values given for REF air mass type in Table 3.
[b]Based on background CO_2 of 372 ppmv and correlation of CO_2 with CO and CH_4.

imately 372 ppmv. This is very close to the average CO_2 level of 371.3 ppmv determined for the TP REF category (Table 3). The correlation between the in situ CO_2 and CO data from the DC-8 and P-3 in the near-Asia Tropical region was found to follow a quadratic relationship with $r^2 = 0.85$, and this relationship was used to estimate a background CO level of 104.0 ppbv when the background CO_2 was 372 ppmv. This is close to the average CO level of 99.3 ppbv found for the REF air mass category. A similar correlation was done between the CO_2 and CH_4 data, and a linear fit was made to the data ($r^2 = 0.60$) to arrive at an estimated background CH_4 level of 1767.7 ppbv at a CO_2 level of 372 ppmv. The average CH_4 value of 1755.0 ppbv in the REF category is somewhat lower than this estimate.

[51] The background fluxes of O_3 and CO were calculated from the average values associated with the REF category, and background fluxes of CO, CO_2, and CH_4 were calculated from the background values estimated from their correlation with CO_2 at a background value of 372 ppmv. These background fluxes were then subtracted from the total flux shown in Table 4 to produce an estimated flux that could be attributed to Asia (Table 5b). Based on using the REF air mass composition as representative of the background conditions, the resulting O_3 flux associated with Asia was 2.3 Tg/day, which represents 41% of the total O_3 flux. Also, the Asian CO flux was estimated at 0.56 Tg/day (0.24 Tg-C/day), which is only 11% of the total CO flux. Based on the CO_2-derived CO background value of 104.0 ppbv, the estimated Asian CO flux was 0.34 Tg/day (0.14 Tg-C/day), which is 39% lower than the estimate using the REF background.

[52] Owing to the high background levels for CO_2 and CH_4, the calculated contribution from Asia is highly dependent on the background value chosen for the analysis, and therefore the CO_2-based background values for CO and CH_4 were assumed to be the best available estimate of the background values. Based on a CO_2 background of 372 ppmv, the Asian CO_2 flux was estimated to be 4.9 Tg-C/day, which is significantly less than the Asian CO_2 flux of 13.9 Tg-C/day estimated by *Vay et al.* [2003]. Some of this difference might be attributed to the latitude and altitude dependent CO_2 background that Vay et al. chose to use and the more limited in situ sampling that was used in their analysis. Using the CO_2-based background value for CH_4, the Asian CH_4 flux was estimated to be only 0.057 Tg-C/day. The CO_2 and CH_4 Asian flux estimates are very sensitive to the background or up-wind gas concentrations. The analyses presented in this section has provided new estimates for the eastward flux of O_3, CO, CO_2, and CH_4 over the western Pacific and an estimate of the contribution of Asia to this flux.

4. Summary and Conclusions

[53] Extensive large-scale distributions of O_3 and aerosol characteristics were obtained from near the surface to above the tropopause on all DC-8 flights during TP. Atmospheric cross sections of O_3, ASR_{IR}, ASR_{VS}, and DPL were derived from a combination of remote and in situ measurements along the aircraft flight track. In situ measurements of O_3 and other trace gases and aerosols were made onboard the DC-8, and the real-time remote O_3 and aerosol lidar measurements and displays were frequently used to guide the in situ sampling strategy. Backward trajectories and meteorological analyses of PV and winds were used extensively in the interpretation of air masses observed during each flight, and several examples were presented here that described the nature of the observed air masses and their possible sources. Large-scale observations of Asian outflow of pollution were found in the low to middle troposphere with enhanced O_3 and aerosols; air from biomass burning regions in SE Asia were seen in the midtroposphere in the tropics with enhanced O_3 and low aerosol loading; and stratospherically influenced air with and without pollution were frequently found with elevated PV levels and elevated O_3. Several case studies were presented for different flights during TP, and the general results of all the observations are summarized below.

[54] Average latitudinal and longitudinal O_3 and ASR_{VS} distributions were determined for TP. Total (stratospheric and tropospheric) and tropospheric cross sections were derived by averaging data from all the TP flights. The average large-scale features of the lower atmosphere over the western Pacific and in different latitude ranges across the Pacific provided insight into the spatial variability in O_3 and aerosol characteristics and the relative influence of various transport and photochemical processes on establishing the observed distributions. The median O_3 and ASR_{VS} in the 0–8-km and 25–46°N region were found to be 58.1 ppbv and 0.74, respectively. The average latitudinal PV distribution was also determined for TP, and the similarities with some of the observed O_3 features were discussed.

[55] The latitudinal distribution of O_3, ASR_{VS}, and PV from PWB was presented and compared with the results from TP. The large-scale differences in O_3 and aerosols between TP and PWB were examined, and it was deter-

mined in the 0–8-km, 25–46°N region that O_3 and ASR_{VS} increased by a median value of 9.4 ppbv (19%) and 0.28 (78%), respectively. The change in the average PV distribution was also examined for the two field experiments, and a significant difference was found which would indicate an increase in STE for TP compared to PWB. This is consistent with the expected STE increase into the spring, and the effect was also seen in the increased frequency of observations of stratospherically influenced air masses. There was also an increase in O_3 and aerosols, without a correlated increase in PV, that are attributed to photochemistry and an increase in pollution outflow, respectively. The average longitudinal distributions of O_3 and aerosols for TP were discussed with respect to different transport and photochemical processes, and it was noted how the O_3 and aerosol levels had increased between PWB and TP for the same reasons as given above for the western Pacific.

[56] An air mass characterization was conducted for all remote O_3 and ASR_{VS} observations made during TP and PWB. Eleven air mass types were defined based on the levels of O_3, ASR_{VS}, and PV-derived stratospheric O_3 in the observed air masses. The frequency of observation of each air mass type with altitude was determined in low (14–25°N) and middle (25–46°N) latitude regions in the western Pacific. In the low-latitude region, the convective outflow/clean Pacific (CON/CP) air mass type was the most frequently observed; however, the enhanced O_3 air mass types were more frequently observed in TP (31%) than during PWB (23%). The largest change was in the HPLM and SINF categories with relative increases of 195 and 73%, respectively. In the midlatitude region, the HPLM and HPLV categories dominated the lower free troposphere in TP (>70%) and to a lesser degree in PWB (<35%). The relative increase in the enhanced O_3 air masses during TP compared to PWB was 54%, and this was attributed to a relative increase for the tropospheric component of 87% and stratospheric component of 35%. This indicates that there was a significant increase in both photochemistry and STE that contributed to the O_3 budget and the differences between the two field experiments.

[57] Average aerosol optical characteristics (ASR_{IR}, ASR_{VS}, WVD, and DPL) were determined for the various observed air mass types, and while no particular surprises were found, this was the first quantitative representation of the optical properties of these air masses. The enhanced O_3 and aerosol categories had significant ASR_{IR} (1.2–1.9) with moderate WVD (1.2–1.7) and enhanced DPL (2.5–6.2%). The amount of aerosols with enhanced DPL in these air masses was surprising, but backward trajectories indicated that some of these air masses had possibly encountered desert dust regions a few days earlier. Examining only the aerosols with higher DPL (>5%) in each category indicated that those aerosols had significantly higher ASR_{IR} (2.9–4.7)), lower WVD (0.7–1.2), and higher DPL (>10%) than the average for all the aerosols in the air mass type. This further supports the presence of dust aerosols in the samples. Comparisons of the TP and PWB aerosol properties support the conclusion that there was more STE and more coupling with continental pollution, including desert dust, during TP.

[58] The chemical composition for the different air mass types was determined for TP and PWB, and it was found that PWB had higher levels of nearly all pollution related gases and aerosols compared to TP. Also, the hydrocarbon ratios indicate that the PWB air masses were less processed than the same air masses observed in TP. These results can be explained by the lower level of photochemical activity that was present during PWB, which was 3 weeks earlier than TP. This conclusion is also supported by the photochemical model analysis by Davis et al. (submitted manuscript, 2003). During TP there was evidence for significant mixing of stratospheric and tropospheric air as indicated by the composition of the HPLM and HPLV air. Even the SINF category showed evidence of tropospheric air mixed into the lower stratosphere during the increasingly active STE exchange that occurs during the springtime (see also Avery et al., submitted manuscript, 2003).

[59] Eastward O_3 flux distributions for TP were estimated for each air mass type from a combination of the air mass characterization results, measured O_3 distributions, and the wind analysis for each flight. The average latitudinal distribution of the O_3 flux for each air mass type reflected the predominant spatial location (latitude and altitude) of the various air masses, and the magnitude of the O_3 flux was dominated by the wind at that location. As a result, the total O_3 flux distribution was maximum near the subtropical jet, and air masses types that were most often observed near the jet were found to have the highest O_3 flux. The HPLV category had the largest O_3 flux near 8 km and 35°N. The column integrated tropospheric O_3 flux showed a peak of 340 Gg/day/deg at 32°N. Between 14 and 46°N, the total O_3 flux was found to be 5.2 Tg/day with HPLV and HPLM representing 47% of the flux. All of the enhanced O_3 categories together represent 78% of the flux, and it is estimated that 58% of the flux was associated with the stratosphere.

[60] Total flux estimates were also made for O_3, CO, CO_2, and CH_4 based on the average gas composition for the different air mass types. The O_3 flux calculated with this approach compared well with the full O_3 flux analysis discussed above. The relative magnitude of the fluxes of these gases in the various air mass types was similar to that for O_3 as a result of the flux being strongly influenced by the wind distribution. Thus the HPLV category had the highest flux for all the gases. CO had an estimated total flux of 5.2 Tg/day (2.2 Tg-C/day), and HPLV and HPLM accounted for 48% of the flux. CO_2 and CH_4 were estimated to have total fluxes of 27×10^3 Tg/day (7.4×10^3 Tg-C/day) and 47 Tg/day (35 Tg-C/day), respectively. In addition, the background fluxes for O_3, CO, CO_2, and CH_4 were estimated and subtracted from the total flux to provide an estimate as to the portion of the total flux that could be attributed to Asia. Based on a CO_2 background value of 372 ppmv, the Asian flux for CO was estimated at 0.14 Tg-C/day. The Asian CO_2 and CH_4 fluxes were also estimated at 4.9 and 0.057 Tg-C/day, respectively; however, it is recognized that these estimates are highly sensitive to the assumed background values for CO_2 and CH_4. These are the first flux estimates for O_3, CO, CO_2, and CH_4 based on remote and in situ gas measurements and wind analysis. Contributions to the flux from the various air mass types allows for an examination of the relative influence of different processes and atmospheric components on the total gas flux.

[61] **Acknowledgments.** The authors thank Anthony Notari, Jerry A. Williams, William J. McCabe, and George V. Insley Jr. at the NASA

Langley Research Center for their assistance in all aspects related to installing, operating, and maintaining the airborne UV DIAL system on the DC-8 during the TP field experiment. We also very much appreciate the cooperation of the NASA Dryden Flight Research Center's DC-8 flight crew in conducting this field experiment. The funding for this investigation came from NASA's Tropospheric Chemistry Program.

References

Bey, I., D. J. Jacob, J. A. Logan, and R. M. Yantosca, Asian chemical outflow to the Pacific in spring: Origins, pathways, and budgets, *J. Geophys. Res.*, *106*, 23,097–23,113, 2001.

Browell, E. V., Remote sensing of tropospheric gases and aerosols with an airborne DIAL system, in *Optical Laser Remote Sensing*, edited by D. K. Killinger and A. Mooradian, pp. 138–147, Springer-Verlag, New York, 1983.

Browell, E. V., A. F. Carter, S. T. Shipley, R. J. Allen, C. F. Butler, M. N. Mayo, J. H. Siviter Jr., and W. M. Hall, NASA multipurpose airborne DIAL system and measurements of ozone and aerosol profiles, *Appl. Opt.*, *22*, 522–534, 1983.

Browell, E. V., S. Ismail, and S. T. Shipley, Ultraviolet DIAL measurements of O_3 profiles in regions of spatially inhomogeneous aerosols, *Appl. Opt.*, *24*, 2827–2836, 1985.

Browell, E. V., et al., Large-scale air mass characteristics observed over the Western Pacific during summertime, *J. Geophys. Res.*, *101*, 1691–1712, 1996a.

Browell, E. V., et al., Ozone and aerosol distributions and air mass characteristics over the South Atlantic Basin during the burning season, *J. Geophys. Res.*, *101*, 24,043–24,068, 1996b.

Browell, E. V., S. Ismail, and W. B. Grant, Differential Absorption Lidar (DIAL) measurements from air and space, *Appl. Phys.-B*, *67*, 399–410, 1998.

Browell, E. V., et al., Large-scale air mass characteristics observed over the remote tropical Pacific Ocean during March–April 1999: Results from PEM Tropics B Field Experiment, *J. Geophys. Res.*, *106*, 32,481–32,501, 2001.

Browell, E. V., et al., Ozone, aerosol, potential vorticity, and trace gas trends observed at high-latitudes over North America, *J. Geophys. Res.*, *108*(D4), 8369, doi:10.1029/2001JD001390, 2003.

Fenn, M. A., E. V. Browell, and C. F. Butler, Airborne lidar measurements of ozone and aerosols during PEM-West A and PEM-West B, in *Advances in Atmospheric Remote Sensing With Lidar*, edited by A. Ansmann et al., pp. 355–358, Springer Verlag, New York, 1997.

Fenn, M. A., et al., Ozone and aerosol distributions and air mass characteristics over the south Pacific during the burning season, *J. Geophys. Res.*, *104*, 16,197–16,212, 1999.

Fuelberg, H. E., C. M. Kiley, J. R. Hannan, D. J. Westberg, M. A. Avery, and R. E. Newell, Meteorological conditions and transport pathways during the Transport and Chemical Evolution over the Pacific (TRACE-P) experiment, *J. Geophys. Res.*, *108*(D20), 8782, doi:10.1029/2002JD003092, in press, 2003.

Gregory, G. L., J. T. Merrill, M. C. Shipham, D. R. Blake, G. W. Sachse, and H. B. Singh, Chemical characteristics of tropospheric air over the Pacific Ocean as measured during PEM-West B: Relationship to Asian outflow and trajectory history, *J. Geophys. Res.*, *102*, 28,275–28,285, 1997.

Heald, C. L., D. J. Jacob, P. I. Palmer, M. J. Evans, G. W. Sachse, H. B. Singh, and D. R. Blake, Biomass burning emission inventory with daily resolution: Application to aircraft observations of Asian outflow, *J. Geophys. Res.*, *108*(D21), 8811, doi:10.1029/2002JD003082, in press, 2003.

Hoell, J. M., D. Davis, S. C. Liu, R. Newell, M. Shipham, H. Akimoto, R. J. McNeal, R. J. Bendura, and J. W. Drewry, Pacific exploratory Mission-West A (PEM-West A): September–October 1991, *J. Geophys. Res.*, *101*, 1641–1653, 1996.

Hoell, J. M., D. D. Davis, S. C. Liu, R. E. Newell, H. Akimoto, R. J. McNeal, and R. J. Bendura, The Pacific Exploratory Mission West phase B: February–March 1994, *J. Geophys. Res.*, *102*, 28,223–28,239, 1997.

Jacob, D. J., J. A. Logan, and P. P. Murti, Effect of rising Asian emissions on surface ozone in the United States, *Geophys. Res. Lett.*, *26*, 2175–2178, 1999.

Jacob, D. J., J. H. Crawford, M. M. Kleb, V. E. Conners, R. J. Bendura, J. L. Raper, G. W. Sasche, J. Gille, L. Emmons, and J. C. Heald, The Transport and Chemical Evolution over the Pacific (TRACE-P) mission: Design, execution, and first results, *J. Geophys. Res.*, *108*(D20), 8781, doi:10.1029/2002JD003276, in press, 2003.

Jaffe, D., Transport of Asian air pollution to North America, *Geophys. Res. Lett.*, *26*, 711–714, 1999.

Koike, M., et al., Export of anthropogenic reactive nitrogen and sulfur compounds from the East Asia region in spring, *J. Geophys. Res.*, *108*(D20), 8789, doi:10.1029/2002JD003284, in press, 2003.

Kotchenruther, R. A., D. A. Jaffe, and L. Jaegle, Ozone photochemistry and the role of peroxyacetyl nitrate in the springtime northeastern Pacific troposphere: Results from the Photochemical Ozone Budget of the Eastern North Pacific Atmosphere (PHOBEA) campaign, *J. Geophys. Res.*, *106*, 28,731–28,742, 2001.

Lefer, B., R. Shetter, S. Hall, J. H. Crawford, and J. R. Olson, Impact of clouds and aerosols on photolysis frequencies during TRACE-P: I. Analysis using radiative transfer and photochemical box models, *J. Geophys. Res.*, *108*(D21), 8821, doi:10.1029/2002JD003171, in press, 2003.

Liu, H. Y., D. J. Jacob, L. Y. Chan, S. J. Oltmans, I. Bey, R. M. Yantosca, J. M. Harris, B. N. Duncan, and R. V. Martin, Sources of tropospheric ozone along the Asian Pacific Rim: An analysis of ozonesonde observations, *J. Geophys. Res.*, *107*(D21), 4573, doi:10.1029/2001JD002005, 2002.

Liu, H. Y., D. J. Jacob, I. Bey, R. M. Yantosca, B. N. Duncan, and G. W. Sachse, Transport pathways for Asian combustion outflow over the Pacific: Interannual and seasonal variations, *J. Geophys. Res.*, *108*(D20), 8786, doi:10.1029/2002JD003102, in press, 2003.

Mauzerall, D. L., D. Narita, H. Akimoto, L. Horowitz, S. Walters, D. A. Hauglustaine, and G. Brasseur, Seasonal characteristics of tropospheric ozone production and mixing ratios over East Asia: A global three-dimensional chemical transport model analysis, *J. Geophys. Res.*, *105*, 17,895–17,910, 2000.

Miyazaki, Y., K. Kita, Y. Kondo, M. Koike, M. Ko, W. Hu, S. Kawakami, D. R. Blake, and T. Ogawa, Springtime photochemical ozone production observed in the upper troposphere over east Asia, *J. Geophys. Res.*, *108*(D3), 8389, doi:10.1029/2001JD000811, 2002.

Murayama, T., et al., Ground-based network observation of Asian dust events of April 1998 in east Asia, *J. Geophys. Res.*, *106*, 18,345–18,359, 2001.

Perry, K. D., T. A. Cahill, R. C. Schnell, and J. M. Harris, Long-range transport of anthropogenic aerosols to the National Oceanic and Atmospheric Administration baseline station at Mauna Loa Observatory, Hawaii, *J. Geophys. Res.*, *104*, 18,521–18,533, 1999.

Phadnis, M. J., and G. R. Carmichael, Transport and distribution of primary and secondary nonmethane volatile organic compounds in east Asia under continental outflow conditions, *J. Geophys. Res.*, *105*, 22,311–22,336, 2000.

Pickering, K. E., et al., Trace gas transport and scavenging in PEM-Tropics B South Pacific convergence zone convection, *J. Geophys. Res.*, *106*, 32,591–32,607, 2001.

Pierce, R. B., et al., Regional Air Quality Modeling System (RAQMS) predictions of the tropospheric ozone budget over east Asia, *J. Geophys. Res.*, *108*(D21), 8825, doi:10.1029/2002JD003176, in press, 2003.

Pochanart, P., J. Hirokawa, Y. Kajii, H. Akimoto, and M. Nakao, Influence of regional-scale anthropogenic activity in northeast Asia on seasonal variations of surface ozone and carbon monoxide observed at Oki, Japan, *J. Geophys. Res.*, *104*, 3621–3631, 1999.

Richter, D. A., E. V. Browell, C. F. Butler, and N. S. Higdon, Advanced airborne UV DIAL system for stratospheric and tropospheric ozone and aerosol measurements, in *Advances in Atmospheric Remote Sensing with Lidar*, edited by A. Ansmann et al., pp. 395–398, Springer Verlag, New York, 1997.

Sasano, Y., and E. V. Browell, Light scattering characteristics of various aerosol types: Multiple wavelength lidar observations, *Appl. Opt.*, *28*, 1670–1679, 1989.

Staudt, A. C., D. J. Jacob, J. A. Logan, D. Bachiochi, T. N. Krishnamurti, and G. W. Sachse, Continental sources, transoceanic transport, and interhemispheric exchange of carbon monoxide over the Pacific, *J. Geophys. Res.*, *106*, 32,571–32,589, 2001.

Streets, D. G., G. R. Carmichael, M. Amann, and R. L. Arndt, Energy consumption and acid deposition in northeast Asia, *Ambio*, *28*, 135–143, 1999.

Sun, J. M., M. Y. Zhang, and T. S. Liu, Spatial and temporal characteristics of dust storms in China and its surrounding regions, 1960–1999: Relations to source area and climate, *J. Geophys. Res.*, *106*, 10,325–10,333, 2001.

Talbot, R. W., et al., Chemical characteristics of continental outflow from Asia to the troposphere over the western Pacific Ocean during February–March 1994: Results from PEM-West B, *J. Geophys. Res.*, *102*, 28,255–28,274, 1997.

Thompson, A. M., et al., Ozone observations and a model of marine boundary-layer photochemistry during SAGA-3, *J. Geophys. Res.*, *98*, 16,955–16,968, 1993.

Vay, S. A., et al., The influence of regional-scale anthropogenic emissions on CO2 distributions over the western North Pacific, *J. Geophys. Res.*, *108*(D20), 8801, doi:10.1029/2002JD003094, in press, 2003.

Wang, Z. F., H. Ueda, and M. Y. Huang, A deflation module for use in modeling long-range transport of yellow sand over East Asia, *J. Geophys. Res.*, *105*, 26,947–26,959, 2000.

Wild, O., J. Sundet, M. J. Prather, I. S. A. Isaksen, H. Akimoto, E. Browell, and S. Oltmans, CTM ozone simulations for spring 2001 over the western Pacific: Comparisons with TRACE-P lidar, ozonesondes, and TOMS columns, *J. Geophys. Res.*, *108*(D21), 8826, doi:10.1029/2002JD003283, in press, 2003.

Wilkening, K. E., Trans-pacific air pollution: Scientific evidence and political implications, *Water Air Soil Pollut.*, *130*, 1825–1830, 2001.

Xiao, H., G. R. Carmichael, J. Durchenwald, D. Thornton, and A. Bandy, Long-range transport of SO_x and dust in East Asia during the PEM B Experiment, *J. Geophys. Res.*, *102*, 28,589–28,612, 1997.

Yienger, J. J., M. Galanter, T. A. Holloway, M. J. Phadnis, S. K. Guttikunda, G. R. Carmichael, W. J. Moxim, and H. Levy, The episodic nature of air pollution transport from Asia to North America, *J. Geophys. Res.*, *105*, 26,931–26,945, 2000.

B. E. Anderson, M. A. Avery, E. V. Browell, W. B. Grant, J. W. Hair, G. W. Sachse, and S. A. Vay, Atmospheric Sciences, MS-410A, NASA Langley Research Center, Hampton, VA 23681, USA. (Edward.V. Browell@nasa. gov)

E. L. Atlas and A. Fried, Atmospheric Chemistry Division, National Center for Atmospheric Research, Boulder, CO 80307, USA.

K. B. Bartlett, J. E. Dibb, and R. W. Talbot, Institute for the Study of Earth, Oceans, and Space, University of New Hampshire, Durham, NH 03824, USA.

D. R. Blake, Department of Chemistry, University of California, Irvine, Irvine, CA 92717, USA.

V. G. Brackett, C. F. Butler, and M. A. Fenn, Science Applications International Corporation, One Enterprise Parkway, Suite 250, Hampton, VA 23666, USA.

W. H. Brune, Department of Meteorology, Pennsylvania State University, University Park, PA 16802, USA.

H. E. Fuelberg, Department of Meteorology, Florida State University, Tallahassee, FL 32306, USA.

B. G. Heikes, Graduate School of Oceanography, University of Rhode Island, Narragansett, RI 02882, USA.

Y. Hu, Department of Earth, Atmospheric, and Planetary Sciences, Massachusetts Institute of Technology, Cambridge, MA 02139, USA.

D. J. Jacob, Department of Earth and Planetary Science, Harvard University, Cambridge, MA 02138, USA.

S. T. Sandholm and R. J. Weber, Department of Earth and Atmospheric Sciences, Georgia Institute of Technology, Atlanta, GA 30332, USA.

H. B. Singh, NASA Ames Research Center, Moffett Field, CA 94035, USA.